Decoding natural astrocyte rhythms: dynamic actin waves result from environmental sensing by primary rodent astrocytes

Kate M. O'Neill[1]†, Emanuela Saracino[2]†, Barbara Barile[3], Nicholas J. Mennona[1,4], Maria Grazia Mola[3], Spandan Pathak[1], Tamara Posati[2], Roberto Zamboni[2], Grazia P. Nicchia[3], Valentina Benfenati[2*], Wolfgang Losert[1,4*]

[1] Inst. for Physical Science and Technology, Univ. of Maryland, College Park, MD, USA
[2] Inst. of Organic Synthesis and Photoreactivity, National Research Council of Italy, Bologna, Italy
[3] Dept. of Biosciences, Biotechnology and Biopharmaceutics, Univ. of Bari Aldo Moro, Bari, Italy
[4] Physics Dept., Univ. of Maryland, College Park, MD, USA

† equal contributions as co-first authors
** valentina.benfenati@isof.cnr.it and wlosert@umd.edu (equal contributions as co-corresponding authors)*

Abstract

Astrocytes are key regulators of brain homeostasis, an important physiological process that includes but is not limited to buffering of extracellular K^+, equilibrating osmotic gradients, regulating pH, uptake of neurotransmitters, and releasing growth factors – all of which are essential for proper cognitive function. While previous studies have revealed how specific molecular components of the astrocytic cytoskeleton affect the efficacy of these homeostatic processes, none have studied how homeostasis is linked to the excitable systems character of the cytoskeleton. As recently discovered, excitability of the actin cytoskeleton manifests in second-scale dynamic fluctuations and acts as a sensor of chemo-physical environmental cues. Here we find that homeostatic regulation may be more active than previously thought, involving the excitable dynamics of actin in certain subcellular regions, especially near the cell boundary. Our results further indicate that actin dynamics concentrates into "hotspot" regions that selectively respond to certain chemo-physical stimuli, specifically the homeostatic challenges of ion or water concentration increases. Substrate topography makes the actin dynamics of astrocytes weaker. Superresolution images demonstrate that surface topography is also associated with predominant perpendicular alignment of actin filaments near the cell boundary whereas flat substrates result in an actin cortex mainly parallel to the cell boundary. Additionally, co-culture with neurons increases both the probability of actin dynamics and the strength of hotspots. The excitable systems character of actin thus makes astrocytes direct participants in neural cell network dynamics.

Keywords: astrocytes, actin, cytoskeleton, dynamics, co-culture

Introduction

The ability of the brain to receive and compute information depends on the unique abilities of its component brain cells. After each neuronal action potential, the concentrations of ions and water are altered in the perineural and perivascular spaces. Specifically, the concentration of potassium in these areas may be as high as 60-100 mM [1-3] in pathophysiological situations. One of astrocytes' homeostatic functions is to balance extracellular potassium concentration through potassium uptake and spatial buffering [4-12]. This process relies on the sodium/potassium pump (Na^+/K^+ ATPase), potassium channels from the inward rectifier superfamily, and gap junctional coupling. Moreover, this transmembrane flux of K^+ is also accompanied by osmotically-driven water movement and intracellular calcium signaling [13-16].

With a stellate morphology [17-19], astrocytic processes contact neurons and blood vessels and therefore play critical roles in coupling the neuronal with the vascular activities of the brain [20]. Perisynaptic astrocytic processes (PAPs) and perivascular astrocytic processes (PvAPs) represent functional microdomains and are enriched with water and ion channels that allow astrocytes to precisely control the extracellular environment through continuous sensing and balancing of local ionic changes (between neurons for PAPs and at the blood vessel interface for PvAPs) in response to neuronal network activity [20-26]. At the same time, the gap junctional coupling between astrocytes serves as a signaling mechanism enabling synchronicity and lateral communication between astrocytes within the larger astroglia syncytia [27,28].

Though astrocytic communication via gap junctional coupling enables dynamic exchange between cells at the ionic and molecular scales [1,27-29], questions remain how these small scale dynamics couple with, modulate, and impact responses at larger length scales, such as within astroglial cell networks or the whole brain. In particular, gap junctions participate in potassium spatial buffering by aiding in the dispersion of excess K^+ through the astroglial syncytium [1,4-7] and are also implicated in the propagation of astrocytic calcium waves, a form of extraneuronal signaling [30-34]. The efficiency of these homeostatic processes [35,36] is considered the basis for astrocytes' involvement in cognitive functions while their impairment may cause pathologies ranging from edema to epilepsy [16].

More recently, the importance of astrocytes' structural and functional properties has been highlighted for organ- and system-level functions, including synaptic plasticity, memory formation, learning, and regulation of sleep and metabolic activity [37,38]. Here we investigate the actin cytoskeleton as an integrator from the molecular to the systems scale due to its ability to self-assemble into dynamic networks. Indeed, experiments on fixed cells have revealed the key molecular players regulating changes to astrocyte morphology, including but not limited to Rac1 and RhoA GTPases [39-44] and the Arp2/3 complex [45], all of which play a role in promoting, maintaining, or reversing the stellate morphology typical of differentiated astrocytes [46]. Other recent studies on fixed cells have also indicated that the astrocytic actin cytoskeleton plays a role in several homeostatic processes, such as volume regulation and potassium spatial buffering [47-49].

However, much less is known about the second-scale dynamics of the actin cytoskeleton in these cellular processes. For migrating cells – such as neutrophils, metastatic cancer cells, and even

microglia – actin dynamics had been mostly considered as a facilitator of changes in cell morphology. For example, a recent study in T cells demonstrated the importance of global (whole cell) actin dynamics in facilitating immunological synapse formation [50]. New lines of research, though, are also investigating the importance of actin dynamics in crucial cell processes. Dynamic actin has been shown to be important for biological function [51,52], such as surveillance of the brain parenchyma by microglia [53]. Notably, actin cytoskeletal dynamics are necessary for relaying biomechanical forces at the synapse [54], indicating that mechanical signals (in addition to the well-studied chemical and electrical signals) are critical for synaptic transmission and, therefore, cognitive function.

Moreover, recent studies across multiple cell types have demonstrated that the actin cytoskeleton is not only dynamic when a cell changes shape and moves but is also an excitable system with its own intrinsic dynamics, including sustained waves and oscillations that persist independently of changes to cell shape [55-64]. To this end, we have demonstrated that actin waves serve as sensors of electric field strength and direction in the *D. discoideum* model system [64], and we both suspect and have demonstrated that this role extends to other cell types [63]. The source of actin dynamics is thought to be twofold: i) a cytoskeletal excitable network of proteins (CEN) that drives cycles of polymerization and depolymerization typically lasting a few seconds, and ii) a signal transduction excitable network (STEN) that can self-organize these local oscillations into larger scale waves that drive cell migration [51,58,59,65]. We propose that, in astrocytes, CEN dynamics dominate, thus leading to local actin dynamics that is stationary in space and occurs on a second timescale. Therefore, CEN could carry information about homeostatic challenges that occur at the nanometer, ionic, and molecular scales.

Here we study how the actin cytoskeleton serves as the bridge from these smaller scales (e.g., ions) to larger scales (e.g., cells) and facilitates the global (cellular level) homeostatic response of astrocytes. We analyze actin dynamics using optical flow [60,66] and perform shape analysis [57,67,68] on timelapse images of live primary astrocytes transduced with actin-GFP. We demonstrate that actin dynamics occurs in astrocytes and that it can be triggered by extracellular environment modifications, such as an increase in ion concentrations or a change in culturing environment. The spatial distribution of the actin dynamics is localized near the boundary of the cell and is concentrated into active clusters we term "hotspots".

Notably, the strength of actin dynamics changes depending on whether the exposure is to an increase in extracellular potassium or to hypotonic challenge, abbreviated as "high K^+" and "hypotonic", respectively. We refer to the application of these solutions to cultures as "triggering" conditions because they have been shown to mimic pathophysiological changes in the extracellular milieu similar to epilepsy [69] or edema [70] and to cause responses in astrocytes that range from swelling to calcium waves [3,48,71-78]. In addition, activity identified in the processes of differentiated astrocytes, induced by nanotopography [79], is weaker when compared to polygonal astrocytes, which have the shape characteristic of undifferentiated astrocytes grown in the absence of neurons [80-84]. Surprisingly, astrocytes co-cultured with neurons show more frequent dynamics than polygonal cells, and the dynamics were of comparable magnitude. Finally, superresolution imaging by STimulated Emission Depletion (STED) microscopy and analysis with a filament extraction algorithm demonstrates that the specific orientation of actin filament structures occurs only in differentiated cells, indicating that both structure and dynamics carry

information about the environment. Overall, our results indicate that actin is dynamic in astrocytes and behaves collectively by clustering into "hotspot" regions that respond in distinct ways to specific chemo-physical stimuli and may drive the homeostatic response of the neural cell network.

Results

Primary astrocytes display actin dynamics in response to chemical cues

Our live imaging results demonstrate that astrocytes consistently display actin dynamics, particularly near the boundary of the cell. Representative overlays of fluorescent images are shown in **Fig. 1A** (A1 and inset for representative control timelapse; A2 and inset for representative "triggering" timelapse). In this representation, a perfectly stationary cell would appear all white; the presence of different colors indicates non-overlapping structures at either earlier (more blue) or later (more red) times. To quantify actin dynamics, we employ an optical flow method [85] similar to that used in our previous work [60]. We additionally use shape analysis [57,67,68] to separately consider actin dynamics within the whole cell, boundary region, and bulk region (see **Fig. 1A3-4** for representative analyses and **Fig. 1B** for schematic and *Materials and Methods* for more detail). Still images of actin-GFP and brightfield (separate and merged) are also included (**Fig. 1 – figure supplement 1A**).

To obtain an overall picture of how actin dynamics changes between control and triggering conditions, we first quantified the strength of actin dynamics within specific subcellular regions, specifically the boundary region and bulk region (**Fig. 1C1**). Only triggering with hypotonic causes an increase in the strength of actin dynamics within the boundary region ($p=0.040$ for control vs. hypotonic via paired t-test). We do not observe significant differences in actin dynamics strength within the boundary after triggering with high K^+ ($p=0.147$ for control vs. high K^+ via paired t-test) or within the bulk for either triggering condition ($p=0.696$ and $p=0.052$ for control vs. high K^+ and for control vs. hypotonic, respectively, via paired t-test). Notably, neither of the triggering conditions changes the probability of actin dynamics within the boundary or bulk regions (**Fig. 1 – figure supplement 1B**).

We next wanted to understand whether actin dynamics becomes more probable within the boundary region after a triggering stimulus. To accomplish this, we calculate the fraction of dynamics within the boundary and find a significant shift in actin dynamics towards the boundary after triggering with hypotonic but not after triggering with high K^+ (**Fig. 1C2**; $p=0.881$ and $p=0.013$ for control vs. high K^+ and for control vs. hypotonic, respectively, as determined by paired t-test).

To delve into distance dependence of actin dynamics more closely, we quantify the distance from instances of actin dynamics to the cell boundary (true boundary shown in **Fig. 1B**). Curves of the representative cells shown in **Fig. 1A** are shown in **Fig. 1D1** with the boundary and bulk regions labeled. Since we are most interested in the high actin activity near the boundary, we compare how the probability of actin dynamics changes over distance when comparing the two triggering conditions to their matched controls. High K^+ cells display no difference in actin dynamics at specific distances within the boundary region (**Fig. 1D2**). In contrast, hypotonic cells are

178 significantly more likely to show actin dynamics within the boundary region compared to matched
179 controls, specifically between 1.44 and 2.52 μm from the boundary ($p<0.05$ for control vs.
180 hypotonic, for as determined by repeated measures ANOVA; refer to **Fig. 1D3** legend for exact p-
181 values). Taken together with the data from **Fig. 1C2**, we show that a higher probability of actin
182 dynamics at specific distances after hypotonic challenge is indeed accompanied by an overall shift
183 to the boundary region.
184
185 These results indicate the following: i) actin dynamics has a higher probability of occurring under
186 hypotonic conditions (**Fig. 1C1**); ii) increased probability of actin dynamics at specific distances
187 is observed when cells are exposed to hypotonic challenge (**Fig. 1D3**); and iii) this increase at
188 specific distances after hypotonic challenge is also reflected in the overall probability of actin
189 dynamics (**Fig. 1 – figure supplement 1B**) and in the shift of actin dynamics to the boundary
190 (**Fig. 1C2**).
191
192 Finally, we also used inhibitors of the inwardly rectifying K^+ channel Kir4.1 (barium [Ba^{2+}]) and
193 of gap junctions (carbenoxolone [CBX]), involved respectively in potassium spatial
194 buffering [86,87] and cell volume regulation in astrocytes [88,89], to provide a more mechanistic
195 view of how chemical triggering with high K^+ and hypotonic media changes actin dynamics. These
196 inhibitors decrease actin dynamics such that robust analysis was not possible (representative
197 fluorescent overlays and analysis provided in **Fig. 1 – figure supplement 2**). Future studies will
198 attempt to study the effects of these inhibitors when actin dynamics are in a more excited state.
199
200

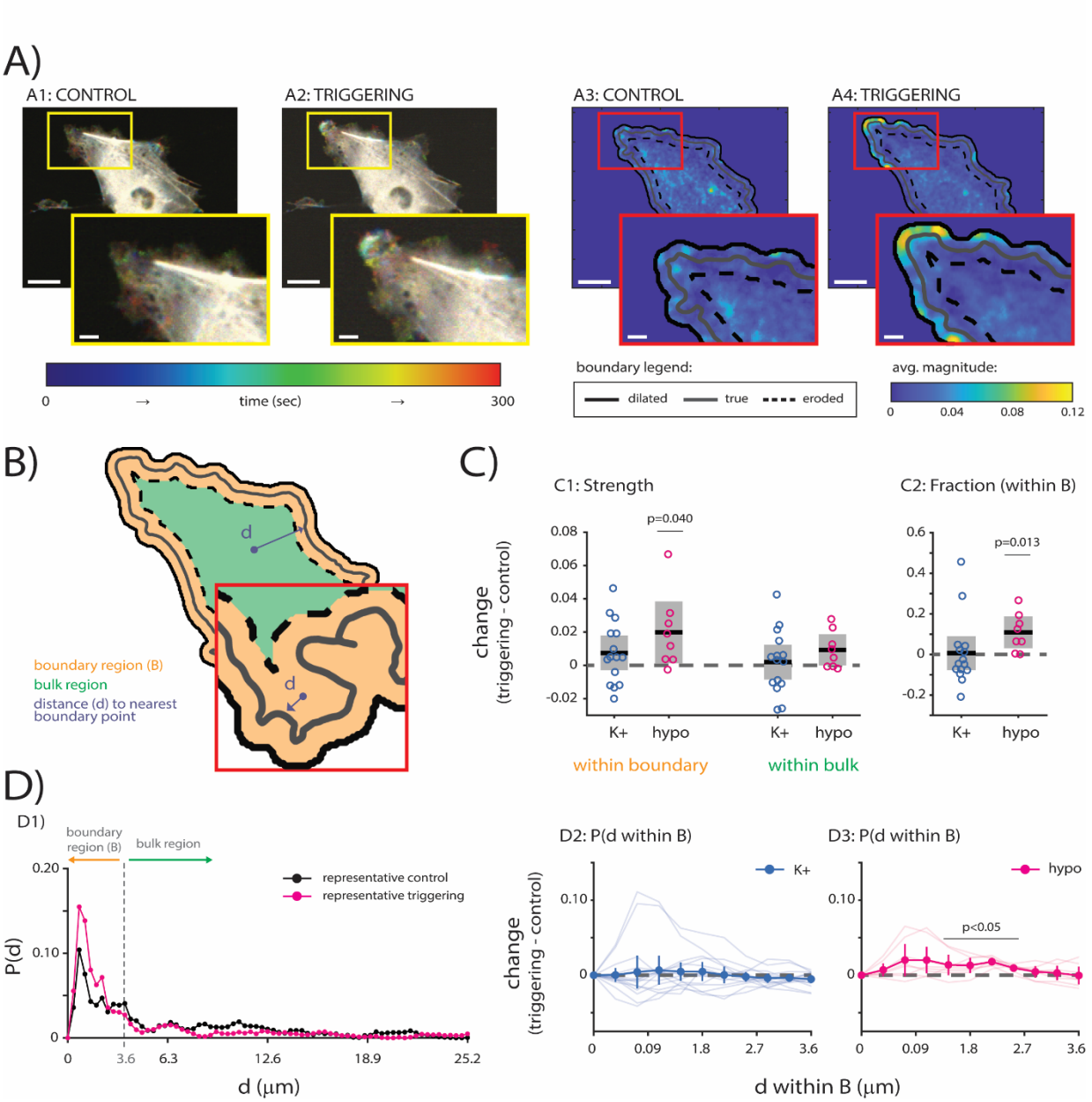

Fig. 1 Optical flow analysis reveals actin dynamics in primary astrocytes
A) Representative actin dynamics. Actin-GFP timelapse overlay for representative cell, control (A1 and inset) and triggering (A2 and inset) conditions. Colorbar indicates time. Optical flow analysis for representative cell: control (A3 and inset) and triggering (A4 and inset) conditions. Colorbar indicates average optical flow magnitude. **B)** Shape analysis [57,67,68] identifies true boundary (solid grey line). Boundary region (orange) is created by dilating (solid black line) and eroding (dashed black line) true boundary by 10 pixels and is distinct from bulk region (green). **C)** Characterizing actin dynamics. **C1)** Strength of actin dynamics within boundary (p=0.147 for control vs. K+, p=0.040 for control vs. hypo) and within bulk (p=0.696 for control vs. K+, p=0.052 for control vs. hypo). **C2)** Fraction of actin dynamics within boundary (p=0.881 for control vs. K+, p=0.013 for control vs. hypo). **D)** Distance dependence of actin dynamics. **D1)** Probability *P(d)* vs. distance from boundary *d* for representative data

shown in B. **D2-D3)** Probability within boundary region *P(d within B)* vs. distance from true boundary within boundary region *d within B* for all cells for control vs. K+ (D2) and for control vs. hypo (D3; p=0.0499, p=0.019, p<0.001, p<0.001 at 1.44-2.52 μm). P-values determined by paired t-test (C) or by repeated measures ANOVA (D). n=15 paired cells for control vs. K+, and n=8 paired cells for control vs. hypo. Scalebars indicate 20 μm (A1-A4) or 5 μm (insets). Error bars/boxes indicate 95% confidence intervals. Solid black lines and opaque circles indicate mean. Transparent lines in D2-D3 represent individual distance curves. "Control" indicates cells imaged in standard external medium; "triggering" indicates cells imaged in isotonic high potassium solution ("K+") or hypotonic solution ("hypo").

Actin dynamics within astrocytes is clustered into active "hotspot" regions

While characterizing actin dynamics within astrocytes, we noticed that many cells seemed to have active regions near the boundary (**Fig. 2A1**) that we suspected were responsible for most of the actin dynamics. To identify these "hotspot" regions, we apply the image processing techniques of erosion and dilation to identify areas of persistent activity (**Fig. 2A2**). After applying thresholds for activity magnitude and probability and hotspot size, we segment regions that meet these criteria (**Fig. 2A3** and inset).

We first compared the strength of actin dynamics within the hotspot regions, considering the boundary and bulk regions separately as before. In contrast to what we found in **Fig. 1C1** (stronger actin dynamics in the boundary region after hypotonic challenge), we find within hotspot regions that actin dynamics is stronger only in cells exposed to high K^+ and only within the boundary region (**Fig. 2B1**; boundary: p=0.006 for control vs. high K^+ and p=0.435 for control vs. hypotonic as determined by paired t-test; bulk: p=0.339 for control vs. high K^+ and p=0.298 for control vs. hypotonic as determined by paired t-test).

We also investigated the relative strength of hotspot dynamics where the average magnitude within hotspots is normalized by the average magnitude of dynamics within the whole cell (**Fig. 2B2**). When comparing this relative strength between cells in triggering conditions and their matched controls, we find that only high K^+ cells display significantly stronger actin dynamics within hotspot regions compared to the whole cell (p=0.006 for control vs. high K^+ and p=0.639 for control vs. hypotonic as determined by paired t-test). Finally, we investigated whether actin dynamics in these hotspot regions is more persistent and find that the duration is not significantly different for either high K^+ cells or hypotonic cells compared to matched controls (**Fig. 2B3**; p=0.056 for control vs. high K^+ and p=0.491 for control vs. hypotonic as determined by paired t-test).

To complement the results investigating strength and relative strength, we also quantified probability and relative probability for the hotspots after chemical triggers. We find that the probability of actin dynamics in hotspots within the boundary does not change for either stimulus (p=0.969 for control vs. high K^+ and p=0.557 for control vs. hypotonic as determined by paired t-test), though the probability of dynamics within bulk region hotspots significantly decreases after hypotonic challenge (p=0.847 for control vs. high K^+ and p=0.027 for control vs. hypotonic as determined by paired t-test; **Fig. 2 – figure supplement 1A**). For both chemical triggers, there is

no relative change in probability within hotspots (p=0.215 for control vs. high K^+ and p=0.462 for control vs. hypotonic as determined by paired t-test; **Fig. 2 – figure supplement 1B**).

To provide a static visualization of actin dynamics within these hotspots, we show traditional actin fluorescence kymographs (**Fig. 2C1**) and novel actin dynamics kymographs (**Fig. 2C2**) for the three largest hotspot regions (red, orange, and yellow) in the representative cell. Both types of kymographs clearly show stronger dynamics in the triggering condition. Moreover, while not evident in the kymograph shown, we also find that cells triggered by high K^+ show a significant decrease in the number of hotspots (p=0.021 for control vs. high K^+ and p=0.189 for control vs. hypotonic; **Fig. 2 – figure supplement 1C**) and a concomitant increase in the average area of hotspots (p=0.047 for control vs. high K^+ and p=0.794 for control vs. hypotonic; **Fig. 2 – figure supplement 1D**), indicating that nearby hotspots may have merged in the high potassium environment. Taken together, these results show that i) hotspot regions respond differently to chemically triggering stimuli than does the subcellular region in which they reside (**Fig. 2B1-B2**) and ii) they are specifically reactive to the high K^+ chemical stimulus in terms of strength of dynamics and both number and average area of hotspots (**Fig. 2 – figure supplement 1C-D**).

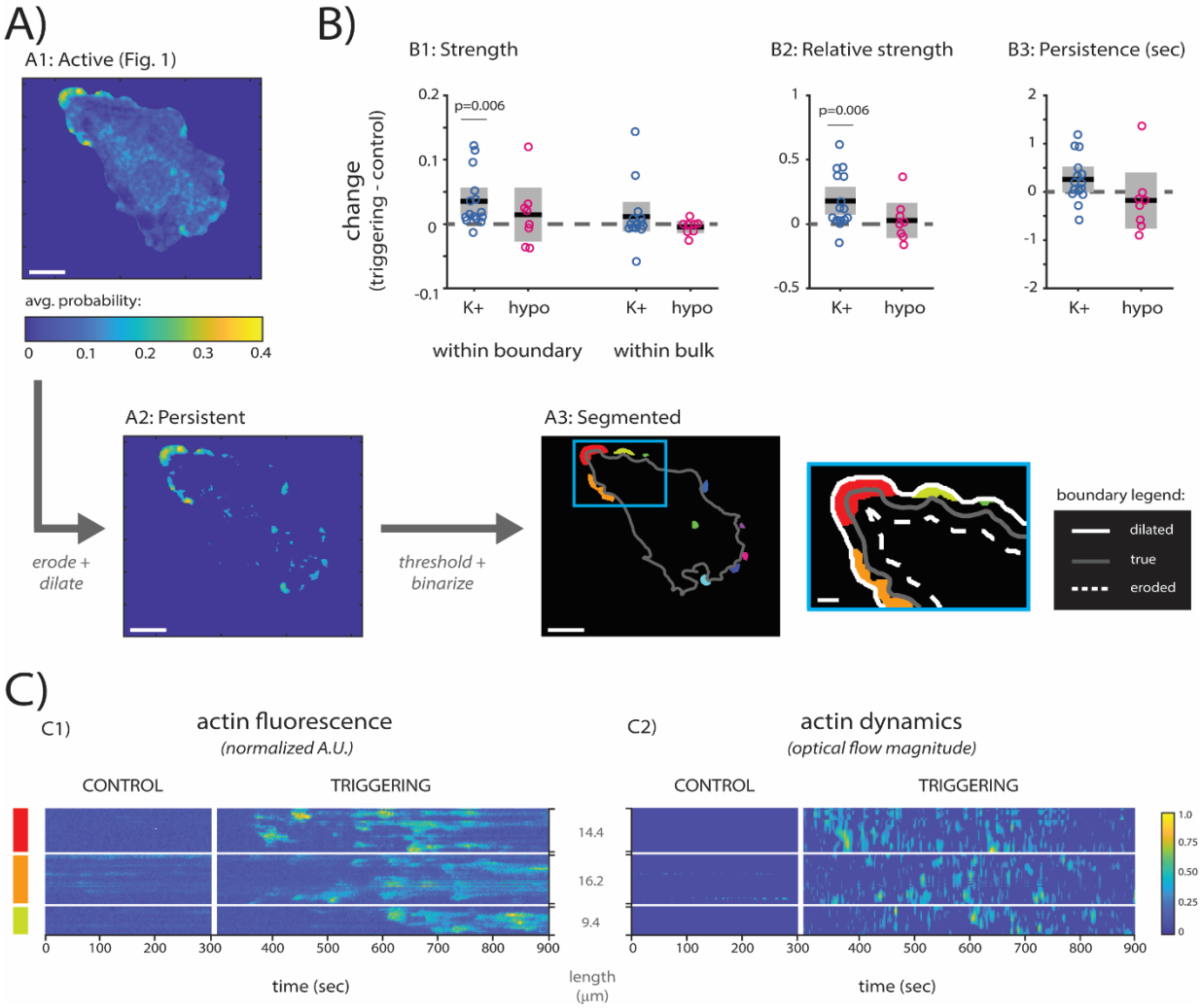

Fig. 2 Persistence analysis of actin dynamics reveal "hotspots" of actin activity
A) Identification of "hotspot" regions. Optical flow results (A1; from Fig. 1) are eroded and dilated in space and in time (A2) to identify the most persistently active regions. Regions that meet criteria are binarized and segmented (A3, inset A4) for comparison between cells and conditions. **B)** Characterization of hotspot dynamics. **B1)** Average strength of hotspot actin dynamics within boundary (p=0.006 for control vs. K+, p=0.435 for control vs. hypo) and within bulk (p=0.339 for control vs. K+, =0.298 for control vs. hypo). **B2)** Relative strength of actin dynamics (p=0.006 for control vs. K+, p=0.639 for control vs. hypo). **B3)** Average persistence of actin dynamics (p=0.056 for control vs. K+, p=0.491 for control vs. hypo). All p-values determined by paired t-test. Solid black lines indicate the mean. Grey regions indicate 95% confidence interval. **C)** Kymographs of normalized actin fluorescence (C1) and of optical flow magnitude (C2) for three largest hotspot regions from A3-A4. Grey labels between kymographs indicate lengths of regions. Colorbar indicates normalized fluorescence (C1) and optical flow magnitude (C2). n=15 paired cells for control and K+, and n=8 paired cells for control and hypo.

<u>Astrocytes display distinct actin dynamics in the presence of neurons and nanotopographic cues</u>

To observe actin dynamics in more *in vivo*-like cell culture conditions, we used two different approaches: i) astrocytes plated on a nanostructured surface, with starlike shapes and more realistic molecular and functional features devoted to homeostatic control of potassium concentrations and cell volume [77,79], and ii) co-culture of astrocytes with primary cortical neurons.

For the first approach, we took advantage of the topographic features in hydrotalcyte-like compound (HTlc) films to understand how actin dynamics is altered by mechanical stimuli at the nanometer scale. For the second approach, we transduced primary astrocytes while still in the flask and then added them to cultures of primary neurons to generate a co-culture. The results shown in **Fig. 3** characterize how the actin dynamics of polygonal astrocytes grown on PDL-coated glass ("PDL" or "PDL cells") differ from differentiated astrocytes grown on the nanotopographic surface HTlc ("HTlc" or "HTlc cells") and from astrocytes co-cultured with neurons ("Co" or "Co cells") under control conditions (standard external medium). Representative examples of fluorescence overlays and optical flow analyses for each cell type are shown in **Fig. 3A**. Refer to **Fig. 3 – figure supplement 1A-C** for still images of actin-GFP and brightfield (separate and merged) of astrocytes grown on PDL, on HTlc, and on PDL in the presence of neurons, respectively. Note that the images shown in **Fig. 3 – figure supplement 1A** are the same representative images as those shown in **Fig. 1 – figure supplement 1A**; they are provided again to facilitate comparison between culturing conditions.

In **Fig. 3B,** we first compared how actin dynamics differs in the boundary and bulk regions for PDL cells, HTlc cells, and Co cells. We find that both PDL cells and Co cells show significantly stronger dynamics within the boundary region and within the bulk region compared to HTlc cells (**Fig. 3B1**; $p<0.001$ for HTlc vs. PDL and $p<0.001$ for HTlc vs. Co as determined by one-way ANOVA followed by Tukey's multiple comparisons test). Surprisingly though, when comparing boundary to bulk within each condition (**Fig. 3B2**), we find that all conditions (PDL, HTlc, and

Co) show significantly stronger dynamics at the boundary compared to the bulk ($p<0.001$ for PDL, and $p=0.012$ for HTlc, and $p=0.001$ for Co as determined by paired t-test).

We next compared how likely the different groups of cells are to show actin dynamics in different subcellular regions. Within both the boundary and bulk regions, only Co cells are significantly more likely to show actin dynamics compared to PDL cells (**Fig. 3C1**; $p<0.001$ for boundary and $p=0.003$ for bulk as determined by one-way ANOVA followed by Tukey's multiple comparisons test). The probability of observing dynamics within the boundary and bulk of HTlc cells is not significantly different from either PDL or Co cells (boundary: $p=0.051$ for PDL vs. HTlc and $p=0.082$ for HTlc vs Co; bulk: $p=0.128$ for PDL vs HTlc and $p=0.604$ for HTlc vs Co; all as determined by one-way ANOVA followed by Tukey's multiple comparisons test). In this case, there is no significant difference between probability of dynamics within boundary and bulk for any condition (**Fig. 3C2**; $p=0.072$ for PDL, $p=0.615$ for HTlc, and $p=0.093$ for Co as determined by paired t-test).

Finally, we evaluated distance dependence of actin dynamics under each culturing condition in **Fig. 3D**. We show the full distance curves in **Fig. 3 – figure supplement 1D** for the representative cells. When comparing individual distances within boundary region (**Fig. 3D1**), we see that only Co cells are significantly more likely to have actin dynamics than PDL cells at specific distances ($p<0.001$ for all distances between 0.72 and 2.16 μm as determined by two-way ANOVA followed by Tukey's multiple comparisons test). Finally, when examining the fraction of events within the boundary (**Fig. 3D2**), we find that PDL cells are less likely to have actin dynamics within the boundary than either HTlc cells and Co cells ($p=0.031$ and $p<0.001$ for PDL vs. HTlc and for PDL vs. Co, respectively, as determined by one-way ANOVA followed by Tukey's multiple comparisons test), with no difference between HTlc and Co cells ($p=0.122$ as determined by one-way ANOVA followed by Tukey's multiple comparisons test). Taken together, these results indicate the following: i) HTlc cells show weaker actin dynamics than both PDL and Co cells with no difference in probability (**Fig. 3B1** and **Fig. 3C1**), ii) Co cells show equally strong and more frequent actin dynamics than PDL cells (**Fig. 3B1** and **Fig. 3C1**), and iii) both HTlc and Co cells show a significant shift in dynamics towards the boundary compared to PDL cells (**Fig. 3D2**).

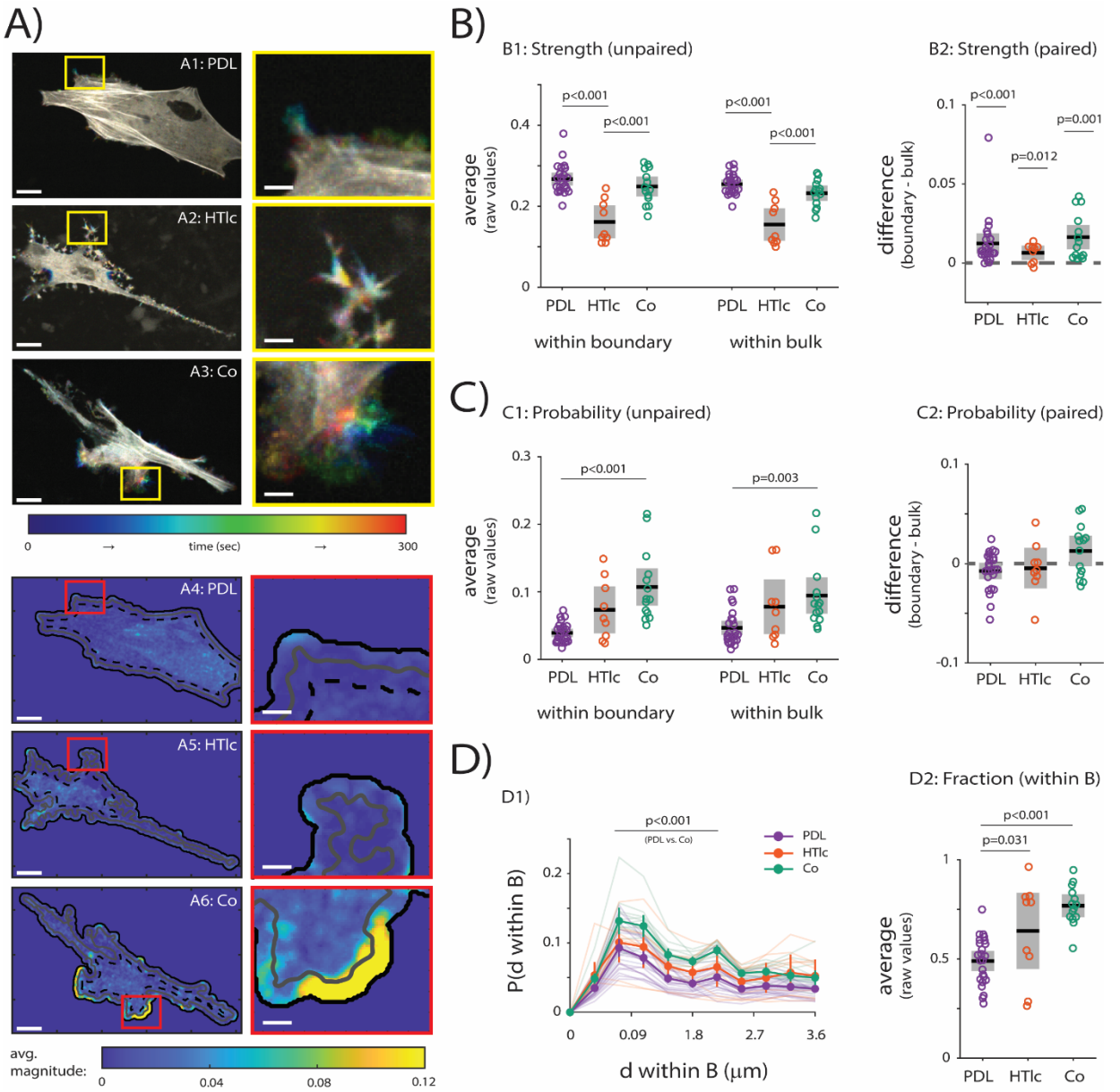

Fig. 3 Actin dynamics differs substantially in polygonal astrocytes grown on PDL compared to differentiated astrocytes grown on HTlc and to astrocytes co-cultured with neurons

A) Actin-GFP timelapse for representative cells grown on PDL-coated glass ("PDL"; A1 and inset), HTlc films ("HTlc"; A2 and inset), and co-cultured with neurons ("Co"; A3 and inset). Colorbar indicates time. Optical flow analysis for representative cells (PDL in A4 and inset; HTlc in A5 and inset; Co in A6 and inset). Colorbar indicates average optical flow magnitude. **B)** Strength of actin dynamics. **B1)** Strength of actin dynamics within boundary ($p<0.001$ for PDL vs. HTlc cells, $p<0.001$ for HTlc vs. Co cells) and within bulk ($p<0.001$ for PDL vs. HTlc cells, $p<0.001$ for HTlc vs. Co cells). **B2)** Strength of actin dynamics in boundary vs. bulk for PDL ($p<0.001$), HTlc ($p=0.011$), and Co cells ($p<0.001$). **C)** Probability of actin dynamics. **C1)** Probability of actin dynamics within boundary ($p<0.001$ PDL vs. Co cells) and within

bulk (p=0.003 for PDL vs. Co cells). **C2)** Probability of actin dynamics in boundary vs. bulk for PDL (p=0.072), HTlc (p=0.615), and Co cells (p=0.093). **D)** Distance dependence of actin dynamics. **D1)** Probability within boundary region *P(d within B)* vs. distance from true boundary within boundary region *d within B* for all PDL, HTlc, and Co cells (p<0.001 at 0.072-2.16 μm for PDL vs. Co). **D2)** Fraction of actin dynamics within boundary (p=0.031 for PDL vs. HTlc, p<0.001 for PDL vs. Co, and p=0.122 for HTlc vs Co). P-values determined by one-way ANOVA followed by Tukey's multiple comparisons test (B1, C1, D2), paired t-test (B2, C2), or two-way ANOVA followed by Tukey's multiple comparisons test (D1). n=24 cells for PDL, n=9 cells for HTlc, and n=14 cells for Co. Scalebars indicate 20 μm (A1-A6) or 5 μm (insets). Error bars/boxes indicate 95% confidence intervals. Solid black lines and opaque circles indicate mean. Transparent lines in D1 represent individual distance curves.

<u>Astrocytes display hotspot regions in the presence of neurons that are more active than in the absence of neurons</u>

We next sought to compare whether hotspot dynamics differed between astrocytes cultured on PDL-coated glass in the absence of neurons (PDL) and in the presence of neurons (Co). Astrocytes grown and differentiated on HTlc did not display consistent hotspot regions for reliable analysis.

Within hotspots, the strength of actin dynamics within the boundary region is significantly stronger in Co cells compared to PDL cells, whereas we observe no difference between PDL and Co cells within the bulk region (**Fig. 4B1**; p=0.003 for PDL vs. Co within boundary and p=0.063 for PDL vs. Co within bulk as determined by two-sample t-test). Additionally, Co cells also show a significant increase in the strength of hotspot dynamics between the boundary and bulk (**Fig. 4B2**; p=0.075 for PDL and p<0.001 for Co as determined by paired t-tests). The relative strength of hotspots within Co cells is also significantly higher than within PDL cells (**Fig. 4B3**; p=0.009 as determined by two-sample t-test).

We next considered probability of dynamics within hotspots under different culturing conditions. The probability of hotspot dynamics is significantly higher for Co cells compared to PDL cells, both within the boundary and within the bulk (**Fig. 4C1**; p<0.001 for PDL vs. Co within boundary and p=0.001 for PDL vs. Co within bulk as determined by two-sample t-test). Co cells also show a significant increase in the probability of boundary over bulk hotspot dynamics (**Fig. 4C2**; p=0.051 for PDL and p=0.005 for Co as determined by paired t-tests). Furthermore, the average persistence of dynamics within the hotspots of Co cells is significantly higher than that of PDL cells (**Fig. 4C3**; p=0.001 as determined by two-sample t-test).

Finally, the relative probability of dynamics is lower in Co cells than in PDL cells (**Fig. 4 – figure supplement 1A**; p=0.011 for PDL vs. Co as determined by two-sample t-test), indicating that astrocytes co-cultured with neurons are generally more active than without neurons but that their hotspots are less relatively active compared to astrocytes without neurons. The number of hotspots does not differ between PDL cells and Co cells (**Fig. 4 – figure supplement 1B**; p=0.333 for PDL vs. Co as determined by two-sample t-test), but the average area of hotspots is increased in Co cells (**Fig. 4 – figure supplement 1C**; p=0.021 for PDL vs. Co as determined by two-sample t-test).

Taken together, we have shown that, when compared to primary astrocytes only, astrocytes co-cultured with neurons have hotspot dynamics that i) are stronger and more frequent within the boundary (**Fig. 4B1** and **Fig. 4C1**), ii) are relatively stronger (**Fig. 4B3**) but relatively less frequent (**Fig. 4D1**), and iii) persist for longer (**Fig. 4C3**).

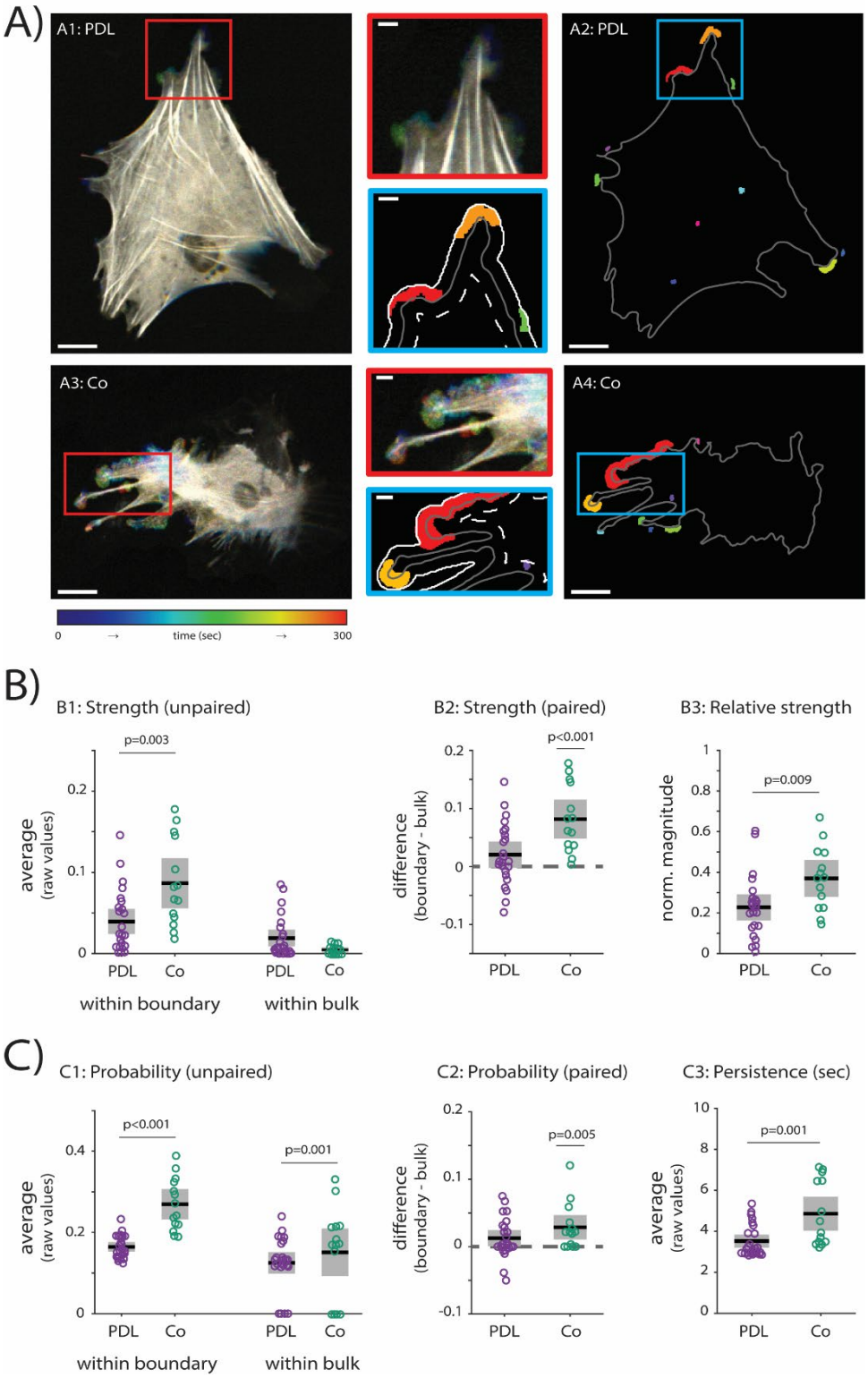

Fig. 4 Actin hotspot dynamics are stronger and more frequent when astrocytes are co-cultured with neurons

A) Actin-GFP timelapse for representative cells grown on PDL-coated glass ("PDL"; A1 and inset) and co-cultured with neurons ("Co"; A3 and inset). Colorbar indicates time. Persistence

analysis for representative cells (PDL in A2 and inset; Co in A4 and inset). Color is used to differentiate hotspot regions. **B)** Strength of actin dynamics within hotspots. **B1)** Strength of hotspot dynamics within boundary (p=0.003 for PDL vs. Co cells) and within bulk (p=0.063 for PDL vs. Co cells). **B2)** Strength of hotspot dynamics in boundary vs. bulk for PDL (p= 0.075) and Co cells (p<0.001). **B3)** Relative strength of hotspot dynamics for PDL vs. Co (p=0.009). **C)** Probability of actin dynamics within hotspots. **C1)** Probability of hotspot dynamics within boundary (p<0.001 for PDL vs. Co cells) and within bulk (p=0.001 for PDL vs. Co cells). **C2)** Strength of actin dynamics in boundary vs. bulk for PDL (p=0.051) and Co cells (p=0.005). **C3)** Persistence of actin dynamics for PDL vs. Co (p=0.001). P-values determined by two-sample t-test (B1, B3, C1, C3) or paired t-test (B2, C2). n=24 cells for PDL, and n=14 cells for Co. Scalebars indicate 20 μm (A1-A4) or 5 μm (insets). Error bars/boxes indicate 95% confidence intervals. Solid black lines and opaque circles indicate mean.

Astrocytes sense nanotopographic cues through actin orientation near the boundary

Inspired by our analysis of actin dynamics in live astrocytes, we sought to understand i) why certain "hotspots" of actin activity are more prevalent in cells grown on PDL than in cells grown on HTlc and ii) whether the characteristics of actin dynamics are related to the underlying actin structure. To this end, we cultured primary rat astrocytes on PDL-coated glass or on HTlc films and performed STED microscopy on fixed cells stained for F-actin and the intermediate filament protein glial fibrillary acid protein (GFAP). Representative images are shown in **Fig. 5**. HTlc preferentially induces stellate morphology characteristic of differentiated astrocytes, whereas astrocytes cultured on PDL-coated glass display the polygonal shapes characteristic of undifferentiated astrocytes grown in the absence of neurons [12,79-84,90]. We chose not to use astrocytes co-cultured with neurons in this portion of our study because overlapping protrusions would have been visualized via immunostaining due to the density of the co-culture, thus preventing robust single-cell analysis. Cell density did not present a technical or analytical challenge for our dynamics data because transduction efficiency is low enough to obtain single cells in the field of view.

Confocal images of F-actin labeled astrocytes reveal that there is a marked tendency for cells grown on PDL (**Fig. 5A**) to display a polygonal and dynamic phenotype with distinct leading and trailing edges and several motile structures (i.e. lamellipodia, filopodia, stress fibers; **Fig. 5C**). Conversely, in the "star" shaped cells grown on HTlc (**Fig. 5B**), the same motile elements that would indicate direction of propagation are not clearly visible (**Fig. 5D**). Moreover, the astrocytic actin is seen to "burst" out of the actin cortex in HTlc cells (**Fig. 5D**). This bursting or "flaring" behavior is indicative of a functional microdomain, known to be present in differentiated astrocytes grown on HTlc [79]. Although many regions in the representative HTlc cell display this microdomain morphology, the actin dynamics of astrocytes plated on HTlc is of lower magnitude than that of astrocytes grown on PDL (refer to **Fig. 3B**). Therefore, we chose to investigate how astrocytic actin senses the different mechanical environments presented by PDL-coated glass and HTlc films and analyze the subsequent cytoskeleton remodeling at a nanoscale level via superresolution imaging. We used a method for quantitative, semi-automated analysis of the actin bundles' preferential orientation [91] to assess the involvement of actin organization in sensing the local mechanical environment around astrocytes.

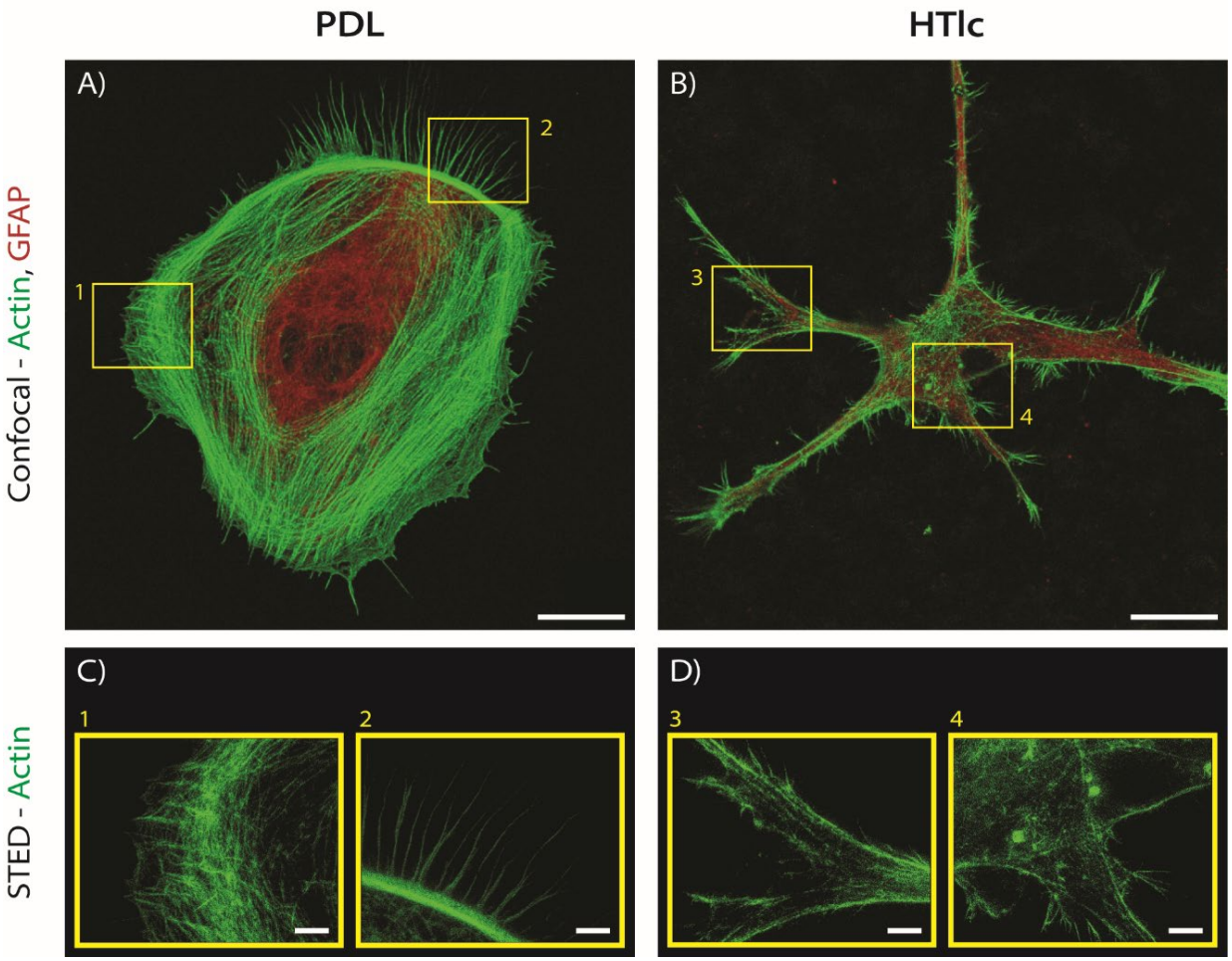

Fig. 5 STED microscopy visualizes nanoscale actin structure within primary astrocytes grown on PDL and on HTlc

A-B) Confocal microscopy images of representative astrocytes grown on PDL-coated glass (A) or on HTlc films (B) for five days, fixed, and stained for actin (green) and GFAP (red). Scalebars indicate 10 µm. **C-D)** Superresolution images taken via STED microscopy of cells grown on PDL (C) and on HTlc (D) of boxed yellow regions from A and B. Scalebars indicate 2.5 µm.

Image analysis was performed by combining segmentation via an anisotropic, rotating Laplacian of gaussian (LoG) kernel with a hierarchical cluster analysis (see **Fig. 6A** for a schematic overview and *Materials and Methods* for a detailed description). These image processing techniques allow for the analysis of actin angle organization and the determination of fractions of actin roughly parallel versus roughly perpendicular to the leading edge of the cell boundary (**Fig. 6B**). From our clustered data, we determine that PDL astrocytic actin is oriented more parallel relative to the leading edge of the astrocyte, whereas HTlc astrocytic actin is oriented more perpendicular

(**Fig. 6C**). The difference seen between the actin of cells grown on PDL versus on HTlc is significant as the cluster algorithm identifies two clusters within the data. Moreover, we see the cluster groups largely correspond with the chosen nanotopography, with an error of seven out of 37 cells: one HTlc cell is misclustered, and six PDL cells are misclustered (i.e., six PDL cells can be found in the cluster of predicted HTlc actin fractions). While the differences observed between astrocytes grown on HTlc and those grown on PDL at a dynamic, micron scale do not necessarily correspond to the differences seen in structure at the nanometer scale, our analytical approach reveals that the underlying nanoscale organization of actin within astrocytes does indeed change when the cells are exposed to different nanotopographic surfaces. Future work will optimize our co-culture approach and determine how the nanoscale structure of astrocytic actin changes when astrocytes are in contact with neurons.

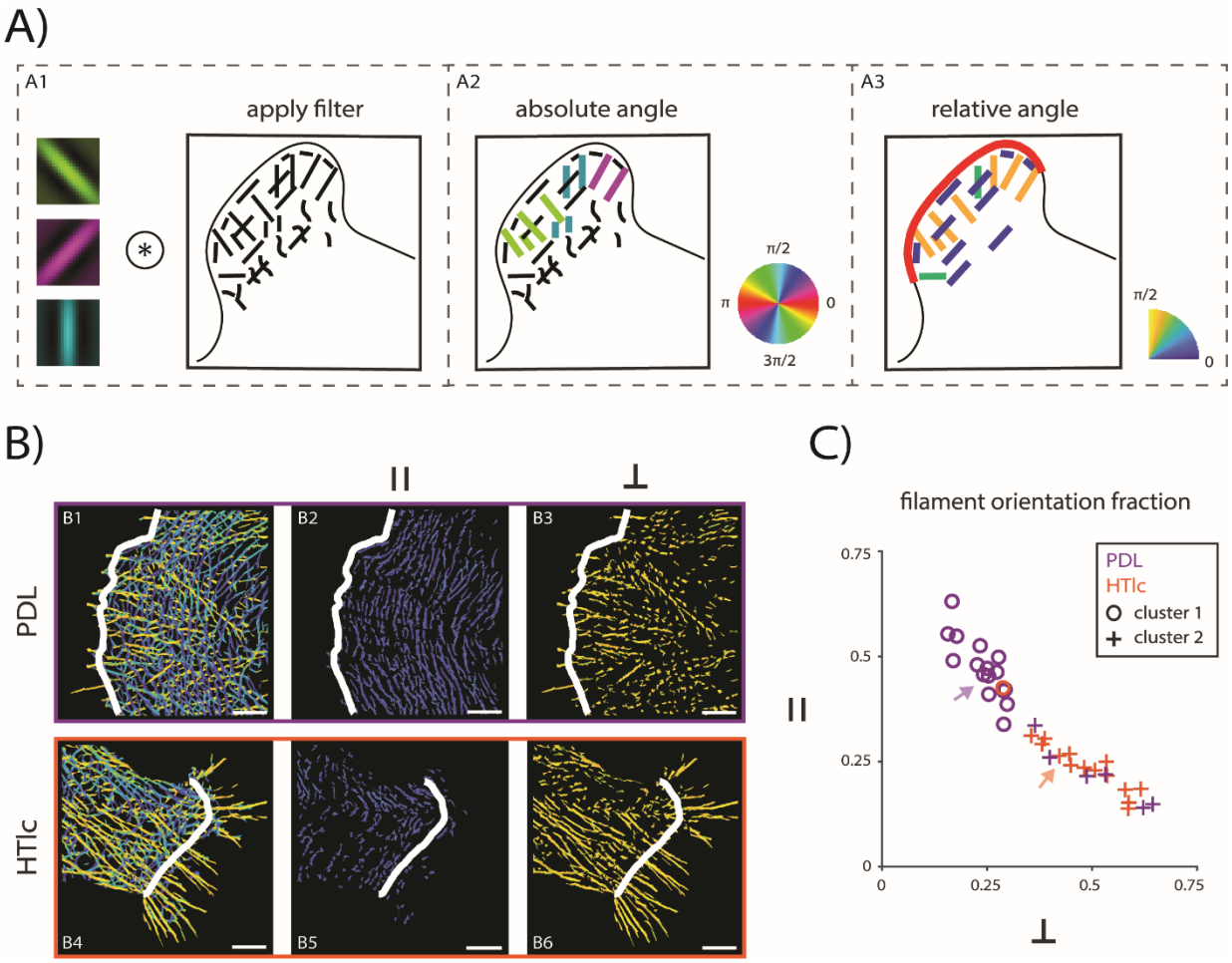

Fig. 6 Filtering STED images with a rotating, anisotropic LoG kernel reveals differences in nanoscale actin structure for astrocytes grown on PDL versus on HTlc

A) Extraction of relative angle information from actin filaments. **A1)** STED images are convolved with a rotating, anisotropic LoG kernel. **A2)** Filtering extracts actin bundles and a best match angle that is relative to the MATLAB frame ("absolute angle") with a range of [0, 2π] (shown as full colorwheel). **A3)** A leading edge boundary (red) is drawn manually and

is used to transform actin angles to be relative to the closes boundary point ("relative angle") with a range of [0, π/2] (shown as a quarter colorwheel). **B)** Output from A for representative cells (PDL in B1-B3, HTlc in B4-B6). All relative angles, parallel angles only (range of [0, π/6]), and perpendicular angles only (range of [π/3, π/2]) for representative PDL (B1, B2, B3, respectively) and HTlc (B4, B5, B6, respectively) cells. Solid white lines indicate leading edge boundary. Scalebars indicate 2.5 μm. **C)** Parallel (y-axis) vs. perpendicular (x-axis) fractions of actin detected within PDL (purple) and HTlc (orange) astrocytes. A hierarchical cluster analysis reveals two distinct clusters (cluster 1: open circles, cluster 2: crosses). Arrows indicate representative cells. n=22 cells for PDL, and n=15 cells for HTlc.

Discussion

We show, for the first time, by means of live timelapse confocal microscopy, that astrocytes respond to alterations in the chemophysical environment with changes in actin dynamics. Furthermore, we demonstrate that actin is spatiotemporally organized into micron scale territories where the dynamics are enhanced depending on the specific chemophysical stress or environment (topography or co-culture). Finally, we show how distinct organization of actin near the boundary may contribute to dynamics.

Our study reveals that actin dynamics occurs persistently and locally, with actin dynamics detectable near the boundary even when the boundary itself does not shift measurably. Hypotonic challenge increases the strength of actin dynamics while high potassium preferentially increases the strength of hotspot dynamics; both changes occur within the boundary region. Furthermore, while astrocytes do not change shape substantially on the short timescales of our experiments, we see small filopodial and lamellopodial structures – the F-actin-rich subcellular compartments of migrating non-neuronal cells [92] – near the cell boundary that appear to "idle" by rapidly extending and retracting, effectively sampling their local environment. It is in these regions, which tend to lack strong stress fibers, that we most often observe actin dynamics. In future experiments, we will quantify how local actin dynamics contribute to changes in astrocyte morphology that occur during differentiation or after injury. Indeed, many studies have extensively demonstrated that, on longer timescales, astrocytes are extremely plastic cells. For example, astrocytes change their morphology by becoming polarized and growing long processes after severe tissue damage caused by traumatic injuries [93-95] and also become hypertrophic and lose their fine processes when they become reactive [19,96].

Surprisingly, dynamics are stronger in astrocytes grown on flat surfaces (PDL-coated glass) and when astrocytes are co-cultured with neurons, clustering into hotspot regions, whereas they are weaker in cells grown on nanostructured surfaces (HTlc films) and do not cluster into large enough regions for hotspot dynamics to be detected with confocal microscopy. Dynamic hotspots in differentiated astrocytes might present as miniature versions of lamellipodia and filopodia, and future work will use higher magnification imaging to determine if this is indeed the case. Importantly, the co-culture results demonstrate that actin dynamics is not highly sensitive to plating density because the co-culture plates were higher in density than the plates with astrocytes only (whether cultured on PDL or HTlc).

564 Our STED data might also provide the key to understanding why polygonal astrocytes display
565 more robust cytoskeleton dynamics: a more parallel and dispersed organization of actin fibers into
566 a meshwork underneath the cell membrane is likely to confer mechanical plasticity to the plasma
567 membrane compared to differentiated cells grown on HTLc, where actin fibers are packed into
568 "actin rails" and not only maintain the cell shape (especially in the cellular processes) but also
569 might cause membrane stiffness or resistance to motility. In support of our hypothesis, a recent
570 study demonstrated increased stiffness at the leading edge of migrating astrocytes using live STED
571 and atomic force microscopy [97]. We also hypothesize that this distinct actin structure will lead
572 to differences in the interaction with neighboring cells. As stellation enables communication with
573 other cell types, perpendicular actin may ensure processes are directed along the proper axis for
574 communication. Indeed, recent work implicates membrane-bound integrins, specifically astrocytic
575 integrin-engaged Thy1, in interacting with the neuronal cytoskeleton to promote astrocyte-neuron
576 communication [98]. Moreover, our finding that almost all cells cultured on HTlc have actin
577 structures perpendicular to the boundary affirms the ability of HTlc to encourage stellate
578 morphology and differentiation of astrocytes [79]. Our analysis also hints that some cells grown
579 on PDL have actin structures that "look" like the actin structures of stellate, differentiated cells
580 grown on HTlc, consistent with previous observations that growth of astrocytes on PDL delays but
581 does not fully suppress spontaneous or gliotic differentiation that might occur in standard cell
582 culture [48,79,99,100].
583
584 Previous studies demonstrated that astrocytes grown on HTlc are more efficient in their
585 homeostatic process. In particular, the expression and function of Kir4.1 and water channel
586 aquaporin 4 (AQP4) as well as the functional response to anisotonic challenge are enhanced in
587 differentiated [77,79] and mature [101-106] cells. A more efficient response to homeostatic
588 challenges due to the higher levels of channel proteins may be related to the weaker actin dynamics
589 observed in differentiated cells compared to polygonal cells (both with and without neurons).
590 While we have not directly investigated this question, a direct relationship between channel
591 function and cytoskeleton dynamics would not be surprising, if we consider that astrocytes may
592 harness the excitable dynamics of actin to codify and convey information coming from the
593 extracellular milieu. Indeed, in fixed cells, it has been shown that the actin cytoskeleton affects
594 AQP4 localization [47,107], but how real time actin dynamics affects the localization and function
595 of AQP4 and other channels, including Kir4.1, remains unknown. To this end, future work will
596 reveal whether the function of potassium and water channels is altered in differentiated compared
597 to polygonal astrocytes after homeostatic challenge and whether any differences in channel
598 localization and function are directly tied to the dynamic response of actin.
599
600 Much is known about how co-culturing astrocytes with neurons alters neuronal function [108-
601 111], but how are astrocytes affected by the presence of neurons? Several studies have shown that
602 the presence of neurons and neuronal activity controls gene expression in astrocytes [80,112,113]
603 and affects astrocytic calcium dynamics [114,115]. For example, rat cortical astrocytes express
604 glutamate-aspartate transporter (GLAST), but in the presence of cortical neurons, as we have done
605 here, astrocytes also express glutamate transporter-1 (GLT-1) [80,113]. Neurons have also been
606 shown to enhance astrocytic expression of Cx43, gap junctional communication between
607 astrocytes, and the propagation of calcium waves within the astrocytic network [116]. We
608 hypothesize that actin dynamics in astrocytes co-cultured with neurons is enhanced specifically
609 because actin dynamics contributes to astrocytes' critical function of facilitating neuronal activity

610 by interacting with neurons and sensing the extracellular environment. Recent work has indicated
611 that actin-dependent morphology changes in PAPs are not only critical for interacting with neurons
612 but may also enhance spine stability [117]. Future work will probe more deeply into how astrocytic
613 actin dynamics affect and may sense the functional dynamics of astrocyte-neuron networks.
614 Indeed, our recent work has shown that actin waves in *D. discoideum* can sense electric fields [64].
615 We will, in the future, investigate whether actin dynamics in astrocytes can also sense and respond
616 to the electrical activity of neurons.
617
618 These questions remain to be elucidated, and studies in microglia [53] – which demonstrated that
619 actin dynamics is critical for their principal function, surveillance – indicate that actin dynamics
620 also plays an important role *in vivo* in neural cells. We propose that actin dynamics in astrocytes
621 is critical for astrocytes' principal functions: maintaining homeostasis and modulating neuronal
622 communication. Finally, given that cytoskeletal alterations are reported in a variety of neurological
623 conditions characterized by a gliotic state [118], we expect investigations of cytoskeletal dynamics
624 in defined animal models to be an important area of exploration to validate the pathophysiological
625 relevance [119] of our findings.
626
627 Moreover, while we know that the astrocyte-neuron interactions will happen on a spatial scale
628 much smaller than the dynamics observed here, our hypothesis is supported by a recent study
629 highlighting the importance of mechanical signaling for synaptic activity [54]. We therefore intuit
630 that astrocytic actin dynamics may serve as a mechanical regulator of neuronal activity.
631
632
633 **Materials and Methods**
634
635 Rat cortical astrocyte culture preparation, maintenance, plating, and differentiation
636
637 *Cell culture:*
638 Primary astrocytes were obtained from Sprague Dawley rats housed at the University of Maryland
639 (in concordance with the recommendations of and approval by the University of Maryland
640 Institutional Animal Care and Use Committee; protocols R-JAN-18-05 and R-FEB-21-04) or from
641 Wistar rats housed at the University of Bologna (in concordance with the Italian and European law
642 of protection of laboratory animals and the approval of the local bioethical committee, under the
643 supervision of the veterinary commission for animal care and comfort of the University of Bologna
644 and approved protocol from Italian Ministry of Health; ethical protocol number ID 360/2017 PR,
645 released on May 2017, valid for 5 years).
646
647 Primary cultures of astrocytes were prepared as described by McCarthy and de Vellis [120] from
648 newborn rat pups between postnatal days 1 and 2 [14,121,90]. Briefly, neonatal cerebral cortices
649 devoid of meninges were gently triturated, filtered with a 70 μm cell strainer (**cat. no. 22-363-548**;
650 Fisher Scientific, MA, USA), and plated in T25 cell culture flasks (**cat. no. 229331**; CELLTREAT
651 Scientific Products, MA, USA) containing Dulbecco's Modified Eagle Medium with GlutaMAX
652 and high glucose (DMEM; **cat. no. 10-566-024**; Fisher Scientific, MA, USA) supplemented with
653 15% fetal bovine serum (FBS; **cat. no. 100-106**; Gemini Bio-Products, CA, USA) and penicillin-
654 streptomycin (P/S) at 100 U/mL and 100 μg/mL, respectively (P/S; **cat. no. 15070063**; Thermo
655 Fisher Scientific, MA, USA). Flasks were maintained in an incubator at 37 °C, 5% CO_2, and proper

656 humidity levels for two weeks. During this period, we replaced cell medium every two days, and
657 flasks were gently shaken when necessary to remove undesired microglial cells. When confluence
658 was reached, astrocytes were dispersed using trypsin-EDTA 0.25% (**cat. no. 25200056**, Thermo
659 Fisher Scientific, MA, USA), and the cell suspension was re-plated on coverslips or in imaging
660 dishes functionalized with Poly-D-lysine hydrobromide (PDL; **cat. no. P7886**; Sigma-Aldrich,
661 MO, USA) as previously described [79,121-124] or with HTlc as previously described [79,125].
662 Cells were plated at a density of $5\text{-}10\times10^3$ per imaging dish and maintained in DMEM containing
663 10% FBS and 1% P/S.
664
665 For co-culture experiments, astrocytes were prepared as described above. At one to two weeks
666 after the astrocyte dissection, neurons were prepared as previously described from rats at
667 embryonic day of gestation 18 (E18) [126-131]. Briefly, embryos were removed via Caesarian
668 section and decapitated. Cerebral hemispheres were separated, and meninges were removed. The
669 hippocampi and cortices were dissected, and cortices were combined and manually triturated.
670 Cortical neurons were plated in imaging dishes coated with PDL at a density of 5×10^5 cells/dish
671 and were maintained in NbActiv4 medium (**cat. no. Nb4-500**, BrainBits, TN, USA) with 1% P/S.
672 When astrocyte flasks reached confluence, astrocytes were added to the neuronal culture at a
673 density of $1\text{-}2\times10^5$ cells/dish, and the media was changed to DMEM with 10% FBS and 1% P/S.
674
675 As can be seen in **Fig. 1 – figure supplement 1A** and **Fig. 3 – figure supplement 1A-C**, plating
676 density was chosen to ensure that cultures were not confluent (which would prevent reliable
677 transduction) and also that astrocytes were not isolated (which could affect dynamics).
678
679 *PDL and HTlc film preparation:*
680 Plastic dishes with glass inserts (**cat. no. P35G-1.0-20-C**, MatTek, MA, USA) or glass coverslips
681 were functionalized with PDL to serve as a control surface or with Zn-Al hydrotalcite nanoparticles
682 (HTlc) to induce morphological differentiation of astrocytes. For live imaging, PDL was used at a
683 working concentration of 0.1 mg/mL. For STED imaging, PDL was used at a working
684 concentration of 0.01 mg/mL. In both cases, coverslips were coated with PDL for 20 minutes at
685 room temperature and washed three times with approximately 500 μL of sterile H_2O. Coverslips
686 or dishes were functionalized with HTlc by adding the HTlc suspension drop by drop on the
687 coverslips and allowed to dry overnight. Once dried, the HTlc coverslips were sterilized by UV
688 for approximately 30 min. For live imaging, astrocytes grown on PDL and HTlc were cultured for
689 three to seven days after replating prior to imaging, and co-cultured astrocytes were cultured for
690 two to three days prior to imaging. For co-culture imaging, neurons were between 4 and 18 days
691 *in vitro*. For STED imaging, astrocytes were cultured for five days after replating prior to fixation.
692
693 Transduction of cells with actin-GFP
694 To visualize actin dynamics, we chose to transduce astrocytes with CellLight Actin-GFP, BacMam
695 2.0 (**cat. no. C10506**; ThermoFisher Scientific, MA, USA) because it has minimal toxicity and
696 sparsely labels cells, which is ideal for single cell analysis. For PDL and HTlc cells, transduction
697 occurred in the imaging dish at a concentration of 100 particles per cell (PPC). At 48 hr prior to
698 live imaging, 5-10 μL (depending on the plating density) of the reagent was added to the cell
699 culture media. A full media change was performed 16-20 hr after transduction, and imaging was
700 performed 24-48 hr after the full media change. For co-cultured astrocytes, transduction occurred
701 in the flask at a concentration of 10 PPC. At 24 hr prior to plating, 100 μL of the reagent was added

to the cell culture medium within the flask. Plating was performed 16-20 hr after transduction. Imaging was performed 48-72 hr after plating.

Live confocal imaging of transduced astrocytes

Live imaging timelapses were acquired at the University of Maryland CMNS Imaging Core using a PerkinElmer spinning disk confocal microscope with an oil immersion 40x objective (1.30 NA; 0.36 µm/pixel) and under temperature, CO_2, and humidity control. The microscope was equipped with a Hamamatsu ImagEM X2 EM-CCD camera (C9100-23B), which recorded 16 bit images. Data acquisition was performed with PerkinElmer's Volocity software (version 6.4.0). A subset of timelapses were taken at the CNR on an inverted confocal microscope (Crisel Instruments) using a 40x water immersion objective (0.16 µm/pixel).

Transduced astrocytes were identified by a positive signal in the 488 nm laser channel. After imaging parameters were set, the media was changed from growth media to standard external solution (control) followed by one of the triggering conditions (high potassium solution or hypotonic solution). Single-plane images were acquired every 2 sec in the 488 channel. A consistent z-plane was assured with Perfect Focus (Nikon PFS).

Immunostaining and superresolution imaging of fixed astrocytes

Antibodies:

Mouse monoclonal Anti-Glial Fibrillary Acidic Protein (GFAP) antibody (diluted 1:200; **cat. no. G3893**; Sigma-Aldrich, MO, USA) and Goat anti-Mouse IgG (H+L) Highly Cross-Adsorbed Secondary Antibody, Alexa Fluor 594 (diluted 1:300; **cat. no. A-11032**; Thermo Fisher Scientific, MA, USA) were used as primary and secondary antibody, respectively, for GFAP immunostaining. Alexa Fluor 488 Phalloidin (diluted 1:500; **cat. no. A12379**; Thermo Fisher Scientific, MA, USA) was used for direct labelling of actin.

STED immunostaining:

Immunofluorescence for gated STED (gSTED) was performed as indicated in the Quick Guide to the STED Sample Preparation (www.leica-microsystems.com), with some slight adjustments as previously reported [132,133]. Astrocytes were plated on the PDL and HTlc-treated coverslips and cultured for five days. On the fifth day of culture, cells were fixed with 2% paraformaldehyde (**cat. no. P6148**; Sigma-Aldrich, MO, USA) in phosphate buffered saline (PBS) for 10 min, washed with PBS, and permeabilized with 0.3% Triton X-100 (**cat. no. T8787**; Sigma-Aldrich, MO, USA) for 10 min. After blocking with 0.1% gelatin in PBS, fixed astrocytes were incubated with GFAP-primary antibody for 1 hr at room temperature. Cells were then rinsed with 0.1% gelatin-PBS and co-incubated with Alexa Fluor 488 Phalloidin and Alexa Fluor 594-conjugated secondary antibody for 1 hr at room temperature. After washing with PBS, coverslips were mounted on microscope slides by using the ProLong Glass Antifade Mountant (**cat. no. P36980**; Thermo Fisher Scientific, MA, USA) without DAPI, as indicated in Leica official guide, and imaged with both confocal and STED microscopy.

STED imaging:

Confocal and STED images of fixed astrocytes grown on PDL and HTlc were acquired using a Leica TCS SP8 3X microscope, provided with AOTF and AOBS, white light laser (WLL), Hybrid

Detectors (HyD), and two STED lasers (592 nm, 660 nm) [133]. A Leica HC PL APO 100x/1.40 NA Oil STED White objective and Type F Immersion liquid with a refractive index of 1.5 were used. Before starting imaging, the excitation and the doughnut-shaped STED beams were switched on (WLL set laser power= 70%; STED-592 nm set laser power = 98%), aligned, and allowed to reach operating temperature. The beam alignment was repeated whenever necessary. Excitation of the Alexa Fluor 488 dye was achieved using a continuous-wave 488 nm laser line (NKT Photonics supercontinuum laser). For superresolution imaging of actin, g-STED was performed using the continuous wave 592 nm-emitting STED fiber laser. More detailed acquisition settings are reported in **Table 1**. All confocal and STED images were acquired at a set room temperature of 20 °C under constant Acquisition Mode settings (Format scanning resolution: 1024x1024 pixels; Scan Speed: 100 Hz).

	Parameter	**Actin**	**GFAP**
Confocal	WLL (488 nm) intensity, %	10	10
	Gain	25	25
STED	WLL (488 nm) intensity, %	40	
	STED (592 nm) intensity, %	97	
	Gain	200	

Table 1: Imaging parameters. Parameters used for STED and confocal imaging of fixed astrocytes on PDL and HTlc.

Criteria for acquisitions of ROIs:

Single or few and well-spaced cells were preferentially chosen for STED imaging to ensure no overlap of actin structure belonging to different cells. Actin and GFAP images of the whole cell were first acquired by confocal microscopy at an original magnification of 100x. Then, multiple random regions of interest (ROIs) (~20x20 µm sized) were selected and imaged using an extra optical zoom (from 5 to 7) by confocal and STED microscopy. Three independent experiments were conducted.

Synthesis of ZnAl-HTlc nanoparticles and film preparation

Colloidal aqueous dispersion of ZnAl-HTlc nanoparticles having the formula $[Zn_{0.72}Al_{0.28}(OH)_2]\,Br_{0.28}\ 0.69\ H_2O$ were prepared by the double-microemulsion technique previously described [79]. For the film preparation, a 125 or 160 µL aliquot of ZnAl-HTlc colloidal dispersion at a concentration of 1.2 mg/mL was dropped onto 15 or 19 mm diameter glass coverslips and successively dried for 4 hr in a sterile hood. The obtained ZnAl-HTlc films were used to culture astrocytes and as substrates for live dynamics imaging and fixed STED imaging as described above. In this manuscript, the ZnAl-HTlc films are referred to simply as HTlc.

785 Solutions and chemicals
786 All salts and chemicals employed for the investigations were of the highest purity grade. For live
787 imaging experiments, the standard external solution ("control") was the following (mM):
788 140 NaCl, 4 KCl, 2 $MgCl_2$, 2 $CaCl_2$, 10 HEPES, 5 glucose, pH 7.4 with NaOH and osmolarity
789 adjusted to ~315 mOsm with mannitol. When using external solutions with different ionic
790 compositions, such as the high potassium solution ("high K^+", [40 Mm]), salts were replaced
791 equimolarly. The hypotonic extracellular solution ("hypotonic") of 260 mOsm/L was obtained by
792 omitting mannitol in the control solution. When imaging, media was changed carefully to prevent
793 accidental, mechanical stimulation of cells with the pipette. Moreover, we controlled for any
794 effects that changing media might cause by changing media prior to imaging under control
795 conditions (from growth media to the standard external solution) and under triggering conditions
796 (from the standard external solution to high K^+ or hypotonic medium).
797
798 Analysis of live imaging data
799
800 *Pre-processing of timelapses:*
801 All timelapses were smoothed in time using a Simoncelli smoothing filter [134]. Prior to
802 smoothing, any timelapses that showed noticeable jitter or drift due to thermal gradients were
803 processed through a jitter correction algorithm using discrete Fourier transform (DFT) registration
804 and an upsampling factor of 100 (using the "dftregistration" code package from [135]). For
805 timelapses where drift was inconsistent and unable to be fully corrected with the DFT method, an
806 additional correction using intensity-based image registration (via the MATLAB functions
807 "imregconfig" and "imregister") was applied using the average image of the DFT corrected
808 timelapse as the fixed image.
809
810 *Shape analysis and identification of bulk and boundary regions:*
811 We used shape analysis to identify cell boundaries and subsequently to be able to compare actin
812 dynamics within different regions of astrocytes. Using a snake algorithm from our previous
813 work [57,67,68], we analyzed the average fluorescent image of each cell to generate the "true
814 boundary" (**see Fig. 1A-B**). Prior to shape analysis, images were smoothed ("imgaussfilt" in
815 MATLAB with a standard deviation of 1.0) and subsequently sharpened ("imsharpen" in
816 MATLAB with a radius of 2.5 and amount of 1.0). Alpha and beta parameters for the snake
817 algorithm (tension and rigidity, respectively) were 0.20 and 0.25, respectively. We found that this
818 true boundary tended to capture the most prominent morphological features of the cell but often
819 excluded regions that were only transiently dynamic. To mitigate this challenge, we eroded or
820 dilated the true boundary using a spherical structural element with a radius of 10 pixels. By
821 subtracting the eroded cell region from the dilated cell region, we identified a boundary region.
822 We considered the eroded cell mask to be the bulk region.
823
824 *Optical flow analysis of actin dynamics:*
825 Optical flow analysis similar to that used in [60] was performed on smoothed and jitter-corrected
826 timelapses in Python 3.8. The optical flow weight matrix was a 19x19 pixel Gaussian with a
827 standard deviation of 3 pixels (1.1 μm) for all timelapses taken at UMD. For a small subset of
828 HTlc timelapses taken at the CNR, the optical flow weight matrix was a 41x41 pixel Gaussian
829 with a standard deviation of 6.75 pixels (1.1 μm). The truncation value for the Gaussian kernel
830 was consistently set to 3. Because actin dynamics in astrocytes is less prominent than in migrating

831 cells usually studied by our lab [56,60], we only considered optical flow vectors with the highest
832 1% of magnitude within the dilated cell boundary that also passed our reliability criteria (at least
833 33% of the mean reliability value for that timelapse). These strict criteria ensured that we were
834 only considering dynamic actin events that are large and reliable compared to background noise.
835
836 *Segmentation of active regions ("hotspots") of actin dynamics:*
837 To identify regions with the most actin activity, we further analyzed our thresholded data by
838 eroding and dilating in the x, y, and time dimensions using an elongated cube with dimensions of
839 [3,3,2]. To ensure that we were not including regions of low activity, we set an event probability
840 threshold of 0.10, meaning that a region had to be active at least 10% of the time to be considered
841 a "hotspot". Furthermore, we imposed a size constraint of 20 pixels (including the time dimension)
842 to ensure that any active regions did not just barely meet the volume require of 3x3x2. Since the
843 dynamics within HTlc cells are on a smaller scale, the hotspot analysis did not reveal any regions
844 that were clearly active.
845
846 Analysis of STED images of fixed astrocytes
847
848 *Laplacian of Gaussian (LoG) filtering to segment actin:*
849 To characterize the organization of the actin meshwork in STED images of fixed cells, as shown
850 in **Fig. 5**, we performed several image processing techniques using custom-written algorithms in
851 MATLAB (Mathworks). Prior to processing, all STED images are adjusted using a contrast-
852 limited adaptive histogram equalization ("adjusthisteq" function in MATLAB's proprietary API
853 (https://www.mathworks.com/help/images/adaptive-histogram-equalization.html). The resolution
854 of the STED images is 16.18pix/nm. Next, each image is convolved with an anisotropic, rotating
855 Laplacian of Gaussian (LoG) kernel. The exact kernel parameters were determined through trial
856 and error to approximately match the cylindrical shape of actin as visualized by Phalloidin-488
857 staining. The number of angles through which the LoG kernel is rotated was chosen to balance
858 computational time and segmentation accuracy. For each pixel, the best match angle is chosen via
859 the maximum value resulting from convolving that pixel with all rotations of the filter, and a
860 threshold is applied to ensure a high-quality match. This processing results in a filtered image that
861 highlights both the actin organization and the angle associated with each filament extracted from
862 kernel (see **Fig. 5A1**). The angles associated with the extracted actin are defined in terms of the
863 Cartesian coordinate system, which is not biologically meaningful. To establish the angle at which
864 the actin organizes relative to the cellular boundary, we manually draw a boundary for each cell.
865 The number of pixels per boundary varies on a cell-to-cell basis. For each pixel, we derive the
866 angle of that pixel's actin relative to the closest boundary point. This transformation generates
867 angles in the range of 0 to $\pi/2$. We then apply an additional threshold at an arbitrary value to only
868 segment the longest actin (**Fig. 5A2**); doing so greatly reduces the noise in our processed data. We
869 analyzed at least 15 individual cells per nanotopographic surface, and the morphologies of the
870 imaged areas varied from cell to cell. Thus, the boundaries are generated to normalize the
871 distributions of the relative angles across the data sets. We noticed that for the STED images taken
872 of astrocytes grown on HTlc, there is more total boundary per unit-area. Thus, the boundaries from
873 which the relative angles are calculated are drawn to coincide with only the leading edge of the
874 cell (see **Fig. 5B** for representative examples).
875
876 *Cluster analysis of relative angles:*

To understand how astrocytic actin organization differs when the cells are grown on different nanotopographies, we use a hierarchical cluster analysis from MATLAB's proprietary API (https://www.mathworks.com/help/stats/cluster-analysis.html). From the relative angle distributions across both PDL and HTlc (22 individual cells and 15 individual cells, respectively), we group the distributions into "parallel" (angles between 0 and $\pi/6$) and "perpendicular" (angles between $\pi/3$ and $\pi/2$), as shown in **Fig. 5B**. As inputs to the clustering algorithm, we use the fractions of "parallel" and "perpendicular" actin of the 37 individual cells but do not include information about the corresponding nanotopographic surface. We then use the "pdist," "linkage," "cophenet," and "linkage" functions (while optimizing the cophenetic coefficient of our 'distance' and 'linkage' parameters) to generate predictive clusters of the input data.

Data representation and statistics

All data were plotted and all statistical tests performed in MATLAB 2021a. For data showing differences between control and triggering or between boundary and bulk regions, paired t-tests were used ("ttest" function in MATLAB). For data in **Fig. 3** comparing PDL to HTlc to Co, one-way analysis of variance (ANOVA) tests were used ("anova1" function). For data in **Fig. 4** comparing PDL to CO, unpaired two-sample t-tests were used ("ttest2" function). When analyzing probability of actin dynamics vs. distance, ANOVA tests were used as follows: repeated measures ANOVA for paired data in **Fig. 1** ("fitrm" and "ranova" functions), and two-way ANOVA to compare PDL to HTlc to Co in **Fig. 3** ("anovan" function). For all ANOVA tests, Tukey's multiple comparisons test ("multcompare" function) was used as the post test. All errorbars indicate 95% confidence interval, and the significance level was set at α=0.05. Adobe Illustrator (version 25.0.1) was used for final assembly of all figures.

Acknowledgements

The authors would like to thank the University of Maryland Imaging Incubator Core Facility for providing and maintaining the systems used in collecting images for this work. They also thank Q. Yang and L. J. Campanello for helpful discussions related to analysis.

Funding

This work was supported by the following grants:

US Air Force Office of Scientific Research MURI grant FA9550-16-1-0052 to WL

US Air Force Office of Scientific Research grant FA9550-19-1-0370 (AstroDyn) to WL VB GPN KMO

US Air Force Office of Scientific Research FA9550-20-1-0386 to (ASTROLIGHT) to VB

US Air Force Office of Scientific Research FA9550-20-1-0324 to GPN

HORIZON EUROPE SEEDS INTERGLIO (S08) funded by the University of Bari Aldo Moro to GPN

NIH R21NS116892-01 to GPN

US Air Force Office of Scientific Research FA9550-18-1-0255 (3D Neuroglia) to VB

COMBINE fellowship to NJM

Author contributions

Conceptualization: VB WL
Surface preparation: ES TP
Experiments: KMO ES BB MGM
Analysis: KMO NJM SP
Interpretation: KMO ES BB NJM MGM GPN VB WL
Supervision: GPN VB WL
Writing—original draft: KMO ES BB NJM GPN VB WL
Writing—review & editing: KMO ES BB NJM MGM SP TP RZ GPN VB WL

Conflict of interest: The authors have no competing interests to declare.

936 **References**

937 1. Scemes E, Spray DC (2012) Extracellular k^+ and astrocyte signaling via connexin and
938 pannexin channels. Neurochemical research 37 (11):2310-2306. doi:10.1007/s11064-012-0759-4

939 2. Somjen GG (1979) Extracellular potassium in the mammalian central nervous system. Annu
940 Rev Physiol 41:159-177. doi:10.1146/annurev.ph.41.030179.001111

941 3. Walz W (1987) Swelling and potassium uptake in cultured astrocytes. Can J Physiol
942 Pharmacol 65 (5):1051-1057. doi:10.1139/y87-166

943 4. Kofuji P, Newman EA (2004) Potassium buffering in the central nervous system.
944 Neuroscience 29 (4):1045-1056. doi:10.1016/j.neuroscience.2004.06.008

945 5. Holthoff K, Witte OW (2000) Directed spatial potassium redistribution in rat neocortex. Glia
946 29(3): (3):288-292. doi:10.1002/(sici)1098-1136(20000201)29:3<288::aid-glia10>3.0.co;2-8

947 6. Orkand RK, Nicholls JG, Kuffler SW (1966) Effect of nerve impulses on the membrane
948 potential of glial cells in the central nervous system of amphibia. J Neurophysiol 29 (4):788-806.
949 doi:10.1152/jn.1966.29.4.788

950 7. Kuffler SW, Nicholls JG, Orkand RK (1966) Physiological properties of glial cells in the
951 central nervous system of amphibia. J Neurophysiol 29 (4):768-787.
952 doi:10.1152/jn.1966.29.4.768

953 8. Baylor DA, Nicholls JG (1969) Changes in extracellular potassium concentration produced by
954 neuronal activity in the central nervous system of the leech. J Physiol 203 (3):555-569.
955 doi:10.1113/jphysiol.1969.sp008879

956 9. Berger T, Schnitzer J, Kettenmann H (1991) Developmental changes in the membrane current
957 pattern, k+ buffer capacity, and morphology of glial cells in the corpus callosum slice. J Neurosci
958 11 (10):3008-3024. doi:10.1523/JNEUROSCI.11-10-03008.1991

959 10. Newman EA (1986) Regional specialization of the membrane of retinal glial cells and its
960 importance to k+ spatial buffering. Ann N Y Acad Sci 481:273-286. doi:10.1111/j.1749-
961 6632.1986.tb27158.x

962 11. Walz W, Wuttke W, Hertz L (1984) Astrocytes in primary cultures: Membrane potential
963 characteristics reveal exclusive potassium conductance and potassium accumulator properties.
964 Brain Res 292 (2):367-374. doi:10.1016/0006-8993(84)90772-8

965 12. Benfenati V, Caprini M, Nobile M, Rapisarda C, Ferroni S (2006) Guanosine promotes the
966 up-regulation of inward rectifier potassium current mediated by kir4.1 in cultured rat cortical
967 astrocytes. J Neurochem 98 (2):430-445. doi:10.1111/j.1471-4159.2006.03877.x

968 13. Parpura V, Verkhratsky A (2012) Neuroglia at the crossroads of homoeostasis, metabolism
969 and signalling: Evolution of the concept. ASN Neuro 4 (4):e00087. doi:10.1042/AN20120019

970 14. Benfenati V, Ferroni S (2010) Water transport between cns compartments: Functional and
971 molecular interactions between aquaporins and ion channels. Neuroscience 168 (4):926-940.
972 doi:10.1016/j.neuroscience.2009.12.017

973 15. Amiry-Moghaddam M, Ottersen OP (2003) The molecular basis of water transport in the
974 brain. Nature reviews 4 (12):991-1001. doi:10.1038/nrn1252

975 16. Bellot-Saez A, Kékesi O, Morley JW, Buskila Y (2017) Astrocytic modulation of neuronal
976 excitability through k+ spatial buffering. Neuroscience and biobehavioral reviews 77:87-97.
977 doi:10.1016/j.neubiorev.2017.03.002

978 17. Oberheim NA, Goldman SA, Nedergaard M (2012) Heterogeneity of astrocytic form and
979 function. Methods Mol Biol 814: 23–45:23-45. doi:10.1007/978-1-61779-452-0_3

980 18. Bushong EA, Martone ME, Jones YZ, Ellisman MH (2002) Protoplasmic astrocytes in ca1
981 stratum radiatum occupy separate anatomical domains. J Neurosci 22 (1):183-192.
982 doi:10.1523/JNEUROSCI.22-01-00183.2002

983 19. Schiweck J, Eickholt BJ, Murk K (2018) Important shapeshifter: Mechanisms allowing
984 astrocytes to respond to the changing nervous system during development, injury and disease.
985 Front Cell Neurosci 12:261. doi:10.3389/fncel.2018.00261

986 20. Boulay AC, Saubaméa B, Adam N, Chasseigneaux S, Mazaré N, Gilbert A, Bahin M,
987 Bastianelli L, Blugeon C, Perrin S, Pouch J, Ducos B, Le Crom S, Genovesio A, Chrétien F,
988 Declèves X, Laplanche JL, Cohen-Salmon M (2017) Translation in astrocyte distal processes
989 sets molecular heterogeneity at the gliovascular interface. Cell Discov 3:17005.
990 doi:10.1038/celldisc.2017.5

991 21. Yang Y, Gozen O, Watkins A, Lorenzini I, Lepore A, Gao Y, Vidensky S, Brennan J,
992 Poulsen D, Park JW, Jeon NL, Robinson MB, Rothstein JD (2009) Presynaptic regulation of
993 astroglial excitatory neurotransmitter transporter glt1. Neuron 61 (6):880-894.
994 doi:10.1016/j.neuron.2009.02.010

995 22. Sibille J, Pannasch U, Rouach N (2014) Astroglial potassium clearance contributes to short-
996 term plasticity of synaptically evoked currents at the tripartite synapse. J Physiol 592 (1):87-102.
997 doi:10.1113/jphysiol.2013.261735

998 23. Murphy-Royal C, Dupuis J, Groc L, Oliet SHR (2017) Astroglial glutamate transporters in
999 the brain: Regulating neurotransmitter homeostasis and synaptic transmission. J Neurosci Res 95
1000 (11):2140-2151. doi:10.1002/jnr.24029

1001 24. Dallérac G, Zapata J, Rouach N (2018) Versatile control of synaptic circuits by astrocytes:
1002 Where, when and how? Nature reviews 19 (12):729-743. doi:10.1038/s41583-018-0080-6

1003 25. Mazaré N, Oudart M, Cohen-Salmon M (2021) Local translation in perisynaptic and
1004 perivascular astrocytic processes - a means to ensure astrocyte molecular and functional polarity?
1005 J Cell Sci 134 (2):jcs251629. doi:10.1242/jcs.251629

1006 26. Ghézali G, Dallérac G, Rouach N (2016) Perisynaptic astroglial processes: Dynamic
1007 processors of neuronal information. Brain Struct Funct 221:2427-2442

1008 27. Spray DC (1996) Molecular physiology of gap junction channels. Clin Exp Pharmacol
1009 Physiol 23 (12):1038-1040. doi:10.1111/j.1440-1681.1996.tb01165.x

1010 28. De Pina-Benabou MH, Srinivas M, Spray DC, Scemes E (2001) Calmodulin kinase pathway
1011 mediates the k+-induced increase in gap junctional communication between mouse spinal cord
1012 astrocytes. J Neurosci 21 (17):6635-6643. doi:10.1523/JNEUROSCI.21-17-06635.2001

1013 29. Giaume C, Tabernero A, Medina JM (1997) Metabolic trafficking through astrocytic gap
1014 junctions. Glia 21 (1):114-123

1015 30. Venance L, Piomelli D, Glowinski J, Giaume C (1995) Inhibition by anandamide of gap
1016 junctions and intercellular calcium signalling in striatal astrocytes. Nature 376 (6541):590-594.
1017 doi:10.1038/376590a0

1018 31. Finkbeiner S (1992) Calcium waves in astrocytes-filling in the gaps. Neuron 8 (6):1101-
1019 1108. doi:10.1016/0896-6273(92)90131-v

1020 32. Enkvist MO, McCarthy KD (1992) Activation of protein kinase c blocks astroglial gap
1021 junction communication and inhibits the spread of calcium waves. J Neurochem 59 (2):519-526.
1022 doi:10.1111/j.1471-4159.1992.tb09401.x
1023 33. Murphy TH, Blatter LA, Wier WG, Baraban JM (1993) Rapid communication between
1024 neurons and astrocytes in primary cortical cultures. J Neurosci 13(6): (6):2672-2679.
1025 doi:10.1523/JNEUROSCI.13-06-02672.1993
1026 34. Charvériat M, Naus CC, Leybaert L, Sáez JC, Giaume C (2017) Connexin-dependent
1027 neuroglial networking as a new therapeutic target. Front Cell Neurosci 11:174.
1028 doi:10.3389/fncel.2017.00174
1029 35. Verkhratsky A, Nedergaard M (2017) Physiology of astroglia. Physiol Rev 98 (1):239-389.
1030 doi:10.1152/physrev.00042.2016
1031 36. Rose CR, Verkhratsky A (2016) Principles of sodium homeostasis and sodium signalling in
1032 astroglia. Glia 64 (10):1611-1627. doi:10.1002/glia.22964
1033 37. Santello M, Toni N, Volterra A (2019) Astrocyte function from information processing to
1034 cognition and cognitive impairment. Nat Neurosci 22 (2):154-166. doi:10.1038/s41593-018-
1035 0325-8
1036 38. Farhy-Tselnicker I, Boisvert MM, Liu H, Dowling C, Erikson GA, Blanco-Suarez E, Farhy
1037 C, Shokhirev MN, Ecker JR, Allen NJ (2021) Activity-dependent modulation of synapse-
1038 regulating genes in astrocytes. Elife 10:e70514. doi:10.7554/eLife.70514
1039 39. Ramakers GJ, Moolenaar WH (1998) Regulation of astrocyte morphology by rhoa and
1040 lysophosphatidic acid. Experimental cell research 245 (2):252-262. doi:10.1006/excr.1998.4224.
1041 40. Kalman D, Gomperts SN, Hardy S, Kitamura M, Bishop JM (1999) Ras family gtpases
1042 control growth of astrocyte processes. Mol Biol Cell 10 (5):1665-1683.
1043 doi:10.1091/mbc.10.5.1665
1044 41. John GR, Chen L, Rivieccio MA, Melendez-Vasquez CV, Hartley A, Brosnan CF (2004)
1045 Interleukin-1beta induces a reactive astroglial phenotype via deactivation of the rho gtpase-rock
1046 axis. J Neurosci 24 (11):2837-2845. doi:10.1523/JNEUROSCI.4789-03.2004
1047 42. Höltje M, Hoffmann A, Hofmann F, Mucke C, Grosse G, Van Rooijen N, Kettenmann H,
1048 Just I, Ahnert-Hilger G (2005) Role of rho gtpase in astrocyte morphology and migratory
1049 response during in vitro wound healing. J Neurochem 95 (5):1237-1248. doi:10.1111/j.1471-
1050 4159.2005.03443.x
1051 43. Racchetti G, D'Alessandro R, Meldolesi J (2012) Astrocyte stellation, a process dependent on
1052 rac1 is sustained by the regulated exocytosis of enlargeosomes. Glia 60 (3):465-475.
1053 doi:10.1002/glia.22280
1054 44. Suidan HS, Nobes CD, Hall A, Monard D (1997) Astrocyte spreading in response to
1055 thrombin and lysophosphatidic acid is dependent on the rho gtpase. Glia 21 (2):244-252.
1056 doi:10.1002/(sici)1098-1136(199710)21:2<244::aid-glia7>3.0.co;2-6
1057 45. Murk K, Blanco Suarez EM, Cockbill LMR, Banks P, Hanley JG (2013) The antagonistic
1058 modulation of arp2/3 activity by n-wasp, wave2 and pick1 defines dynamic changes in astrocyte
1059 morphology. J Cell Sci 126 (17):3873-3883. doi:10.1242/jcs.125146
1060 46. Brozzi F, Arcuri C, Giambanco I, Donato R (2009) S100b protein regulates astrocyte shape
1061 and migration via interaction with src kinase: Implications for astrocyte development, activation,
1062 and tumor growth. J Biol Chem 284 (13):8797-8811. doi:10.1074/jbc.M805897200

1063 47. Nicchia GP, Rossi A, Mola MG, Procino G, Frigeri A, Svelto M (2008) Actin cytoskeleton
1064 remodeling governs aquaporin-4 localization in astrocytes. Glia 56 (16):1755-1766.
1065 doi:10.1002/glia.20724

1066 48. Benfenati V, Nicchia GP, Svelto M, Rapisarda C, Frigeri A, Ferroni S (2007) Functional
1067 down-regulation of volume-regulated anion channels in aqp4 knockdown cultured rat cortical
1068 astrocytes. Journal of Neurochemistry 100 (1):87-104. doi:10.1111/j.1471-4159.2006.04164.x

1069 49. Nicchia GP, Mola MG, Pisoni M, Frigeri A, Svelto M (2007) Different pattern of aquaporin-
1070 4 expression in extensor digitorum longus and soleus during early development. Muscle Nerve
1071 35 (5):625-631. doi:10.1002/mus.20736

1072 50. Fritzsche M, Fernandes RA, Chang VT, Colin-York H, Clausen MP, Felce JH, Galiani S,
1073 Erlenkämper C, Santos AM, Heddleston JM, Pedroza-Pacheco I, Waithe D, de la Serna JB,
1074 Lagerholm BC, Liu T-L, Chew T-L, Betzig E, Davis SJ, Eggeling C (2017) Cytoskeletal actin
1075 dynamics shape a ramifying actin network underpinning immunological synapse formation.
1076 Science advances 3 (6):e1603032. doi:10.1126/sciadv.1603032

1077 51. Li X, Miao Y, Pal DS, Devreotes PN (2020) Excitable networks controlling cell migration
1078 during development and disease. Semin Cell Dev Biol 100:133-142.
1079 doi:10.1016/j.semcdb.2019.11.001

1080 52. Kumari S, Mak M, Poh YC, Tohme M, Watson N, Melo M, Janssen E, Dustin M, Geha R,
1081 Irvine DJ (2020) Cytoskeletal tension actively sustains the migratory t-cell synaptic contact.
1082 EMBO J 39 (5):e102783. doi:10.15252/embj.2019102783

1083 53. Bernier L-P, Bohlen CJ, York EM, Choi HB, Kamyabi A, Dissing-Olesen L, Hefendehl JK,
1084 Collins HY, Stevens B, Barres BA, MacVicar BA (2019) Nanoscale surveillance of the brain by
1085 microglia via camp-regulated filopodia. Cell Rep 27 (10):2895-2908.e2894.
1086 doi:10.1016/j.celrep.2019.05.010

1087 54. Ucar H, Watanabe S, Noguchi J, Morimoto Y, Iino Y, Yagishita S, Takahashi N, Kasai H
1088 (2021) Mechanical actions of dendritic-spine enlargement on presynaptic exocytosis. Nature 600
1089 (7890):686-689. doi:10.1038/s41586-021-04125-7

1090 55. Vicker MG (2002) F-actin assembly in dictyostelium cell locomotion and shape oscillations
1091 propagates as a self-organized reaction-diffusion wave. FEBS Letters 510 (1-2):5-9.
1092 doi:10.1016/s0014-5793(01)03207-0

1093 56. Sun X, Driscoll MK, Guven C, Das S, Parent CA, Fourkas JT, Losert W (2015) Asymmetric
1094 nanotopography biases cytoskeletal dynamics and promotes unidirectional cell guidance. Proc
1095 Natl Acad Sci U S A 112 (41):12557-12562. doi:10.1073/pnas.1502970112

1096 57. Driscoll MK, Sun X, Guven C, Fourkas JT, Losert W (2014) Cellular contact guidance
1097 through dynamic sensing of nanotopography. ACS Nano 8 (4):3546-3555.
1098 doi:10.1021/nn406637c

1099 58. Edwards M, Cai H, Abubaker-Sharif B, Long Y, Lampert TJ, Devreotes PN (2018) Insight
1100 from the maximal activation of the signal transduction excitable network in dictyostelium
1101 discoideum. Proc Natl Acad Sci U S A 115 (16):E3722-E3730. doi:10.1073/pnas.1710480115

1102 59. Miao Y, Bhattacharya S, Banerjee T, Abubaker-Sharif B, Long Y, Inoue T, Iglesias PA,
1103 Devreotes PN (2019) Wave patterns organize cellular protrusions and control cortical dynamics.
1104 Mol Syst Biol 15 (3):e8585. doi:10.15252/msb.20188585

1105 60. Lee R, Campanello L, Hourwitz M, Alvarez P, Omidvar A, Fourkas J, Losert W (2020)
1106 Quantifying topography-guided actin dynamics across scales using optical flow. Mol Biol Cell
1107 mbcE19110614. doi:10.1091/mbc.E19-11-0614

1108 61. Roy S (2016) Waves, rings, and trails: The scenic landscape of axonal actin. J Cell Biol 212
1109 (2):131-134. doi:10.1083/jcb.201511016

1110 62. Del Signore SJ, Kelley CF, Messelaar EM, Lemos T, Marchan MF, Ermanoska B, Mund M,
1111 Fai TG, Kaksonen M, Rodal AA (2021) An autoinhibitory clamp of actin assembly constrains
1112 and directs synaptic endocytosis. Elife 10:e69597. doi:10.7554/eLife.69597

1113 63. Bull AL, Campanello L, Hourwitz MJ, Yang Q, Zhao M, Fourkas JT, Losert W (2022) Actin
1114 dynamics as a multiscale integrator of cellular guidance cues. Front Cell Dev Biol 10:873567.
1115 doi:10.3389/fcell.2022.873567

1116 64. Yang Q, Miao Y, Campanello LJ, Hourwitz MJ, Abubaker-Sharif B, Bull AL, Devreotes PN,
1117 Fourkas JT, Losert W (2022) Cortical waves mediate the cellular response to electric fields. Elife
1118 11:e73198. doi:10.7554/eLife.73198

1119 65. Pal DS, Li X, Banerjee T, Miao Y, Devreotes PN (2019) The excitable signal transduction
1120 networks: Movers and shapers of eukaryotic cell migration. Int J Dev Biol 63 (8-9-10):407-416.
1121 doi:10.1387/ijdb.190265pd

1122 66. Horn BKP, Schunck BG (1981) Determining optical flow. Artif Intell 17:185-203

1123 67. Driscoll MK, Losert W, Jacobson K, Kapustina M (2015) Spatiotemporal relationships
1124 between the cell shape and the actomyosin cortex of periodically protruding cells. Cytoskeleton
1125 (Hoboken) 72 (6):268-281. doi:10.1002/cm.21229

1126 68. Driscoll MK, McCann C, Kopace R, Homan T, Fourkas JT, Parent C, Losert W (2012) Cell
1127 shape dynamics: From waves to migration. PLoS Comput Biol 8 (3):e1002392.
1128 doi:10.1371/journal.pcbi.1002392

1129 69. Du M, Li J, Wang R, Wu Y (2016) The influence of potassium concentration on epileptic
1130 seizures in a coupled neuronal model in the hippocampus. Cogn Neurodyn 10 (5):405-414.
1131 doi:10.1007/s11571-016-9390-4

1132 70. Pivonkova H, Hermanova Z, Kirdajova D, Awadova T, Malinsky J, Valihrach L, Zucha D,
1133 Kubista M, Galisova A, Jirak D, Anderova M (2018) The contribution of trpv4 channels to
1134 astrocyte volume regulation and brain edema formation. Neuroscience 394:127-143.
1135 doi:10.1016/j.neuroscience.2018.10.028

1136 71. Kimelberg HK, Rutledge E, Goderie S, Charniga C (1995) Astrocytic swelling due to
1137 hypotonic or high k+ medium causes inhibition of glutamate and aspartate uptake and increases
1138 their release. Journal of cerebral blood flow and metabolism : official journal of the International
1139 Society of Cerebral Blood Flow and Metabolism 15 (3):409-416. doi:10.1038/jcbfm.1995.51

1140 72. O'Connor ER, Kimelberg HK, Keese CR, Giaever I (1993) Electrical resistance method for
1141 measuring volume changes in monolayer cultures applied to primary astrocyte cultures. Am J
1142 Physiol 264 (2 Pt 1):C471-478. doi:10.1152/ajpcell.1993.264.2.C471

1143 73. Dallwig R, Vitten H, Deitmer JW (2000) A novel barium-sensitive calcium influx into rat
1144 astrocytes at low external potassium. Cell Calcium 28(4): (4):247-259.
1145 doi:10.1054/ceca.2000.0153

1146 74. Yaguchi T, Nishizaki T (2010) Extracellular high k+ stimulates vesicular glutamate release
1147 from astrocytes by activating voltage-dependent calcium channels. J Cell Physiol 225 (2):512-
1148 518. doi:10.1002/jcp.22231

1149 75. O'Connor ER, Kimelberg HK (1993) Role of calcium in astrocyte volume regulation and in
1150 the release of ions and amino acids. J Neurosci 13 (6):2638-2650. doi:10.1523/JNEUROSCI.13-
1151 06-02638.1993

1152 76. Pangrsic T, Potokar M, Haydon PG, Zorec R, Kreft M (2006) Astrocyte swelling leads to
1153 membrane unfolding, not membrane insertion. J Neurochem 99 (2):514-523. doi:10.1111/j.1471-
1154 4159.2006.04042.x

1155 77. Mola MG, Saracino E, Formaggio F, Amerott AG, Barile B, Frigeri A, Palazzo C, Posati T,
1156 Zamboni R, Caprini M, Nicchia GP, Benfenati V (2021) Cell volume regulation mechanisms in
1157 differentiated astrocytes. Cell Physiol Biochem 55 (S1):196-212. doi:10.33594/000000469

1158 78. Mola MG, Sparaneo A, Gargano CD, Spray DC, Svelto M, Frigeri A, Scemes E, Nicchia GP
1159 (2016) The speed of swelling kinetics modulates cell volume regulation and calcium signaling in
1160 astrocytes: A different point of view on the role of aquaporins. Glia 64(1):139-54 (1):139-154.
1161 doi:10.1002/glia.22921

1162 79. Posati T, Pistone A, Saracino E, Formaggio F, Mola MG, Troni E, Sagnella A, Nocchetti M,
1163 Barbalinardo M, Valle F, Bonetti S, Caprini M, Nicchia GP, Zamboni R, Muccini M, Benfenati
1164 V (2016) A nanoscale interface promoting molecular and functional differentiation of neural
1165 cells. Sci Rep 6:31226. doi:10.1038/srep31226

1166 80. Swanson RA, Liu J, Miller JW, Rothstein JD, Farrell K, Stein BA, Longuemare MC (1997)
1167 Neuronal regulation of glutamate transporter subtype expression in astrocytes. J Neurosci 17
1168 (3):932-940. doi:10.1523/JNEUROSCI.17-03-00932.1997

1169 81. Sensenbrenner M, Labourdette G, Delaunoy JP, Pettmann B, Devilliers G, Moonen G, Bock
1170 E (1980) Morphological and biochemical differentiation of glial cells in primary culture. In:
1171 Giacobini E (ed) Tissue culture in neurobiology. Raven, New York, pp 385-395

1172 82. Pettmann B, Louis JC, Sensenbrenner M (1979) Morphological and biochemical maturation
1173 of neurones cultured in the absence of glial cells. Nature 281 (5730):378-380.
1174 doi:10.1038/281378a0

1175 83. Hertz L, Juurlink BHJ, Szuchet S (1985) Cell cultures. In: Lajtha A (ed) Handbook of
1176 neurochemistry, vol 8. 2 edn. Plenum, New York, pp 603-661

1177 84. Juurlink BH, Hertz L (1985) Plasticity of astrocytes in primary cultures: An experimental
1178 tool and a reason for methodological caution. Dev Neurosci 7 (5-6):263-277.
1179 doi:10.1159/000112295

1180 85. Lucas BD, Kanade T An iterative image registration technique with an application to stereo
1181 vision. In: Proceedings of the 7th International Joint Conference on Artificial Intelligence, San
1182 Francisco, CA, USA, 1981. Morgan Kaufmann Publishers Inc., pp 674-679.
1183 doi:10.5555/1623264.1623280

1184 86. Lopatin AN, Nichols CG (2001) Inward rectifiers in the heart: An update on i(k1). J Mol Cell
1185 Cardiol 33 (4):625-638. doi:10.1006/jmcc.2001.1344

1186 87. Alagem N, Dvir M, Reuveny E (2001) Mechanism of ba(2+) block of a mouse inwardly
1187 rectifying k+ channel: Differential contribution by two discrete residues. J Physiol 534 (Pt.
1188 2):381-393. doi:10.1111/j.1469-7793.2001.00381.x

1189 88. Davidson JS, Baumgarten IM (1988) Glycyrrhetinic acid derivatives: A novel class of
1190 inhibitors of gap-junctional intercellular communication. Structure-activity relationships. J
1191 Pharmacol Exp Ther 246 (3):1104-1107

1192 89. Benfenati V, Caprini M, Nicchia GP, Rossi A, Dovizio M, Cervetto C, Nobile M, Ferroni S
1193 (2009) Carbenoxolone inhibits volume-regulated anion conductance in cultured rat cortical
1194 astroglia. Channels (Austin) 3 (5):323-336. doi:10.4161/chan.3.5.9568

1195 90. Ferroni S, Marchini C, Schubert P, Rapisarda C (1995) Two distinct inwardly rectifying
1196 conductances are expressed in long term dibutyryl-cyclic-amp treated rat cultured cortical
1197 astrocytes. FEBS Lett 367 (3):319-325. doi:10.1016/0014-5793(95)00588-z

1198 91. Campanello L, Traver MK, Shroff H, Schaefer BC, Losert W (2021) Signaling through
1199 polymerization and degradation: Analysis and simulations of t cell activation mediated by bcl10.
1200 PLoS Comput Biol 17 (5):e1007986. doi:10.1371/journal.pcbi.1007986

1201 92. Hirrlinger J, Hülsmann S, Kirchhoff F (2004) Astroglial processes show spontaneous
1202 motility at active synaptic terminals in situ. Eur J Neurosci 20 (8):2235-2239.
1203 doi:10.1111/j.1460-9568.2004.03689.x

1204 93. Schiweck J, Murk K, Ledderose J, Münster-Wandowski A, Ornaghi M, Vida I, Eickholt BJ
1205 (2021) Drebrin controls scar formation and astrocyte reactivity upon traumatic brain injury by
1206 regulating membrane trafficking. Nat Commun 12:1490. doi:10.1038/s41467-021-21662-x

1207 94. Faulkner JR, Herrmann JE, Woo MJ, Tansey KE, Doan NB, Sofroniew MV (2004) Reactive
1208 astrocytes protect tissue and preserve function after spinal cord injury. J Neurosci 24 (9):2143-
1209 2155. doi:10.1523/JNEUROSCI.3547-03.2004

1210 95. Bardehle S, Krüger M, Buggenthin F, Schwausch J, Ninkovic J, Clevers H, Snippert HJ,
1211 Theis FJ, Meyer-Luehmann M, Bechmann I, Dimou L, Götz M (2013) Live imaging of astrocyte
1212 responses to acute injury reveals selective juxtavascular proliferation. Nat Neurosci 16 (5):580-
1213 586. doi:10.1038/nn.3371

1214 96. Sofroniew MV, Vinters HV (2010) Astrocytes: Biology and pathology. Acta
1215 neuropathologica 119 (1):7-35. doi:10.1007/s00401-009-0619-8

1216 97. Curry N, Ghézali G, Kaminski Schierle GS, Rouach N, Kaminski CF (2017) Correlative sted
1217 and atomic force microscopy on live astrocytes reveals plasticity of cytoskeletal structure and
1218 membrane physical properties during polarized migration. Front Cell Neurosci 11:104.
1219 doi:10.3389/fncel.2017.00104

1220 98. Maldonado H, Calderon C, Burgos-Bravo F, Kobler O, Zuschratter W, Ramirez O, Härtel S,
1221 Schneider P, Quest AFG, Herrera-Molina R, Leyton L (2017) Astrocyte-to-neuron
1222 communication through integrin-engaged thy-1/cbp/csk/src complex triggers neurite retraction
1223 via the rhoa/rock pathway. Biochim Biophys Acta Mol Cell Res 1864 (2):243-254.
1224 doi:10.1016/j.bbamcr.2016.11.006

1225 99. Ferroni S, Marchini C, Nobile M, Rapisarda C (1997) Characterization of an inwardly
1226 rectifying chloride conductance expressed by cultured rat cortical astrocytes. Glia 21 (2):217-
1227 227. doi:10.1002/(sici)1098-1136(199710)21:2<217::aid-glia5>3.0.co;2-3

1228 100. Nicchia GP, Frigeri A, Liuzzi GM, Santacroce MP, Nico B, Procino G, Quondamatteo F,
1229 Herken R, Roncali L, Svelto M (2000) Aquaporin-4-containing astrocytes sustain a temperature-
1230 and mercury-insensitive swelling in vitro. Glia 31 (1):29-38. doi:10.1002/(sici)1098-
1231 1136(200007)31:1<29::aid-glia30>3.0.co;2-3

1232 101. Sloan SA, Darmanis S, Huber N, Khan TA, Birey F, Caneda C, Reimer R, Quake SR,
1233 Barres BA, Paşca SP (2017) Human astrocyte maturation captured in 3d cerebral cortical
1234 spheroids derived from pluripotent stem cells. Neuron 95 (4):779-790.e776.
1235 doi:10.1016/j.neuron.2017.07.035

1236 102. Molofsky AV, Deneen B (2015) Astrocyte development: A guide for the perplexed. Glia 63
1237 (8):1320-1329. doi:10.1002/glia.22836

1238 103. Molofsky AV, Krencik R, Ullian EM, Tsai H-h, Deneen B, Richardson WD, Barres BA,
1239 Rowitch DH (2012) Astrocytes and disease: A neurodevelopmental perspective. Genes Dev 26
1240 (9):891-907. doi:10.1101/gad.188326.112

1241 104. Clarke LE, Liddelow SA, Chakraborty C, Münch AE, Heiman M, Barres BA (2018)
1242 Normal aging induces a1-like astrocyte reactivity. Proc Natl Acad Sci U S A 115 (8):E1896-
1243 E1905. doi:10.1073/pnas.1800165115

1244 105. Morel L, Higashimori H, Tolman M, Yang Y (2014) Vglut1+ neuronal glutamatergic
1245 signaling regulates postnatal developmental maturation of cortical protoplasmic astroglia. J
1246 Neurosci 34 (33):10950-10962. doi:10.1523/JNEUROSCI.1167-14.2014

1247 106. Nwaobi SE, Lin E, Peramsetty SR, Olsen ML (2014) DNA methylation functions as a
1248 critical regulator of kir4.1 expression during cns development. Glia 62 (3):411-427.
1249 doi:10.1002/glia.22613

1250 107. Neely JD, Amiry-Moghaddam M, Ottersen O, Froehner SC, Agre P, Adams ME (2001)
1251 Syntrophin-dependent expression and localization of aquaporin-4 water channel protein. Proc
1252 Natl Acad Sci U S A 98 (24):14108-14113. doi:10.1073/pnas.241508198

1253 108. Kuijlaars J, Oyelami T, Diels A, Rohrbacher J, Versweyveld S, Meneghello G, Tuefferd M,
1254 Verstraelen P, Detrez JR, Verschuuren M, De Vos WH, Meert T, Peeters PJ, Cik M, Nuydens R,
1255 Brône B, Verheyen A (2016) Sustained synchronized neuronal network activity in a human
1256 astrocyte co-culture system. Sci Rep 6:36529. doi:10.1038/srep36529

1257 109. Moonen G, Franck G, Schoffeniels E (1980) Glial control of neuronal excitability in
1258 mammals: I. Electrophysiological and isotopic evidence in culture. Neurochem Int 2C:299-310.
1259 doi:10.1016/0197-0186(80)90037-6

1260 110. Grisar T, Franck G, Schoffeniels E (1980) Glial control of neuronal excitability in
1261 mammals: Ii. Enzymatic evidence : Two molecular forms of the (na(+),k(+))-atpase in brain.
1262 Neurochem Int 2C:311-320. doi:10.1016/0197-0186(80)90038-8

1263 111. Perea G, Navarrete M, Araque A (2009) Tripartite synapses: Astrocytes process and control
1264 synaptic information. Trends Neurosci 32 (8):421-431. doi:10.1016/j.tins.2009.05.001

1265 112. Hasel P, Dando O, Jiwaji Z, Baxter P, Todd AC, Heron S, Márkus NM, McQueen J,
1266 Hampton DW, Torvell M, Tiwari SS, McKay S, Eraso-Pichot A, Zorzano A, Masgrau R, Galea
1267 E, Chandran S, Wyllie DJA, Simpson TI, Hardingham GE (2017) Neurons and neuronal activity
1268 control gene expression in astrocytes to regulate their development and metabolism. Nat
1269 Commun 8:15132. doi:10.1038/ncomms15132

1270 113. Ghosh M, Yang Y, Rothstein JD, Robinson MB (2011) Nuclear factor-κb contributes to
1271 neuron-dependent induction of glutamate transporter-1 expression in astrocytes. J Neurosci 31
1272 (25):9159-9169. doi:10.1523/JNEUROSCI.0302-11.2011

1273 114. Pasti L, Volterra A, Pozzan T, Carmignoto G (1997) Intracellular calcium oscillations in
1274 astrocytes: A highly plastic, bidirectional form of communication between neurons and
1275 astrocytes in situ. J Neurosci 17 (20):7817-7830. doi:10.1523/JNEUROSCI.17-20-07817.1997

1276 115. Schipke CG, Kettenmann H (2004) Astrocyte responses to neuronal activity. Glia 47
1277 (3):226-232. doi:10.1002/glia.20029

1278 116. Rouach N, Glowinski J, Giaume C (2000) Activity-dependent neuronal control of gap-
1279 junctional communication in astrocytes. J Cell Biol 149 (7):1513-1526.
1280 doi:10.1083/jcb.149.7.1513

1281 117. Bernardinelli Y, Randall J, Janett E, Nikonenko I, König S, Jones EV, Flores CE, Murai
1282 KK, Bochet CG, Holtmaat A, Muller D (2014) Activity-dependent structural plasticity of
1283 perisynaptic astrocytic domains promotes excitatory synapse stability. Curr Biol 24 (15):1679-
1284 1688. doi:10.1016/j.cub.2014.06.025

1285 118. Muñoz-Lasso DC, Romá-Mateo C, Pallardó FV, Gonzalez-Cabo P (2020) Much more than
1286 a scaffold: Cytoskeletal proteins in neurological disorders. Cells 9 (2):358.
1287 doi:10.3390/cells9020358

1288 119. Tobe BTD, Crain AM, Winquist AM, Calabrese B, Makihara H, Zhao W-n, Lalonde J,
1289 Nakamura H, Konopaske G, Sidor M, Pernia CD, Yamashita N, Wada M, Inoue Y, Nakamura F,
1290 Sheridan SD, Logan RW, Brandel M, Wu D, Hunsberger J, Dorsett L, Duerr C, Basa RCB,
1291 McCarthy MJ, Udeshi ND, Mertins P, Carr SA, Rouleau GA, Mastrangelo L, Li J, Gutierrez GJ,
1292 Brill LM, Venizelos N, Chen G, Nye JS, Manji H, Price JH, McClung CA, Akiskal HS, Alda M,
1293 Chuang D-MM, Coyle JT, Liu Y, Teng YD, Ohshima T, Mikoshiba K, Sidman RL, Halpain S,
1294 Haggarty SJ, Goshima Y, Snyder EY (2017) Probing the lithium-response pathway in hipscs
1295 implicates the phosphoregulatory set-point for a cytoskeletal modulator in bipolar pathogenesis.
1296 Proc Natl Acad Sci U S A 114 (22):E4462–E4471. doi:10.1073/pnas.1700111114

1297 120. McCarthy KD, de Vellis J (1980) Preparation of separate astroglial and oligodendroglial
1298 cell cultures from rat cerebral tissue. J Cell Biol 85 (3):890-902. doi:10.1083/jcb.85.3.890

1299 121. Benfenati V, Toffanin S, Capelli R, Camassa LMA, Ferroni S, Kaplan DL, Omenetto FG,
1300 Muccini M, Zamboni R (2010) A silk platform that enables electrophysiology and targeted drug
1301 delivery in brain astroglial cells. Biomaterials 31 (31):7883-7891.
1302 doi:10.1016/j.biomaterials.2010.07.013

1303 122. Saracino E, Maiolo L, Polese D, Semprini M, Borrachero-Conejo AI, Gasparetto J, Murtagh
1304 S, Sola M, Tomasi L, Valle F, Pazzini L, Formaggio F, Chiappalone M, Hussain S, Caprini M,
1305 Muccini M, Ambrosio L, Fortunato G, Zamboni R, Convertino A, Benfenati V (2020) A glial-
1306 silicon nanowire electrode junction enabling differentiation and noninvasive recording of slow
1307 oscillations from primary astrocytes. Adv Biosyst 4 (4):e1900264. doi:10.1002/adbi.201900264

1308 123. Benfenati V, Ferroni S (2015) Microdynamics of water and ion homeostasis in the brain:
1309 Role of aquaporins and ion channels of astroglial cells. In: Boison D, Masino SA (eds)
1310 Homeostatic control of brain function. Oxford University Press.
1311 doi:10.1093/med/9780199322299.003.0001

1312 124. Benfenati V, Martino N, Antognazza MR, Pistone A, Toffanin S, Ferroni S, Lanzani G,
1313 Muccini M (2014) Photostimulation of whole-cell conductance in primary rat neocortical
1314 astrocytes mediated by organic semiconducting thin films. Adv Healthc Mater 3 (3):392-399.
1315 doi:10.1002/adhm.201300179

1316 125. Borrachero-Conejo AI, Adams WR, Saracino E, Mola MG, Wang M, Posati T, Formaggio
1317 F, De Bellis M, Frigeri A, Caprini M, Hutchinson MR, Muccini M, Zamboni R, Nicchia GP,
1318 Mahadevan-Jansen A, Benfenati V (2020) Stimulation of water and calcium dynamics in

1319 astrocytes with pulsed infrared light. FASEB journal : official publication of the Federation of
1320 American Societies for Experimental Biology 34 (5):6539-6553. doi:10.1096/fj.201903049R

1321 126. Firestein BL, Brenman JE, Aoki C, Sanchez-Perez AM, El-Husseini AE, Bredt DS (1999)
1322 Cypin: A cytosolic regulator of psd-95 postsynaptic targeting. Neuron 24 (3):659-672.
1323 doi:10.1016/s0896-6273(00)81120-4

1324 127. O'Neill KM, Donohue KE, Omelchenko A, Firestein BL (2018) The 3' utrs of brain-derived
1325 neurotrophic factor transcripts differentially regulate the dendritic arbor. Front Cell Neurosci
1326 12:60. doi:10.3389/fncel.2018.00060

1327 128. O'Neill KM, Akum BF, Dhawan ST, Kwon M, Langhammer CG, Firestein BL (2015)
1328 Assessing effects on dendritic arborization using novel sholl analyses. Frontiers in Cellular
1329 Neuroscience 9:285. doi:10.3389/fncel.2015.00285

1330 129. O'Neill KM, Kwon M, Donohue KE, Firestein BL (2017) Distinct effects on the dendritic
1331 arbor occur by microbead versus bath administration of brain-derived neurotrophic factor.
1332 Cellular and Molecular Life Sciences 74 (23):4369-4385. doi:10.1007/s00018-017-2589-7

1333 130. Rodriguez AR, O'Neill KM, Swiatkowski P, Patel MV, Firestein BL (2018) Overexpression
1334 of cypin alters dendrite morphology, single neuron activity, and network properties via distinct
1335 mechanisms. Journal of Neural Engineering 15 (1):016020. doi:10.1088/1741-2552/aa976a

1336 131. Rodriguez AR, Anderson ED, O'Neill KM, McEwan PP, Vigilante NF, Kwon M, Akum
1337 BF, Stawicki TM, Meaney DF, Firestein BL (2021) Cytosolic psd-95 interactor alters functional
1338 organization of neural circuits and ampa receptor signaling independent of psd-95 binding. Netw
1339 Neurosci 5 (1):166-197. doi:10.1162/netn_a_00173

1340 132. De Bellis M, Pisani F, Mola MG, Rosito S, Simone L, Buccoliero C, Trojano M, Nicchia
1341 GP, Svelto M, Frigeri A (2017) Translational readthrough generates new astrocyte aqp4 isoforms
1342 that modulate supramolecular clustering, glial endfeet localization, and water transport. Glia 65
1343 (5):790-803. doi:10.1002/glia.23126

1344 133. de Bellis M, Cibelli A, Mola MG, Pisani F, Barile B, Mastrodonato M, Banitalebi S, Amiry-
1345 Moghaddam M, Abbrescia P, Frigeri A, Svelto M, Nicchia GP (2021) Orthogonal arrays of
1346 particle assembly are essential for normal aquaporin-4 expression level in the brain. Glia 69
1347 (2):473-488. doi:10.1002/glia.23909

1348 134. Simoncelli EP (1994) Design of multi-dimensional derivative filters. Proceedings -
1349 International Conference on Image Processing 1:790-794. doi:10.1109/ICIP.1994.413423

1350 135. Guizar-Sicairos M, Thurman ST, Fienup JR (2008) Efficient subpixel image registration
1351 algorithms. Opt Lett 33:156-158. doi:10.1364/ol.33.000156

1352

1353

1354 **Figure Supplements**

1355

1356

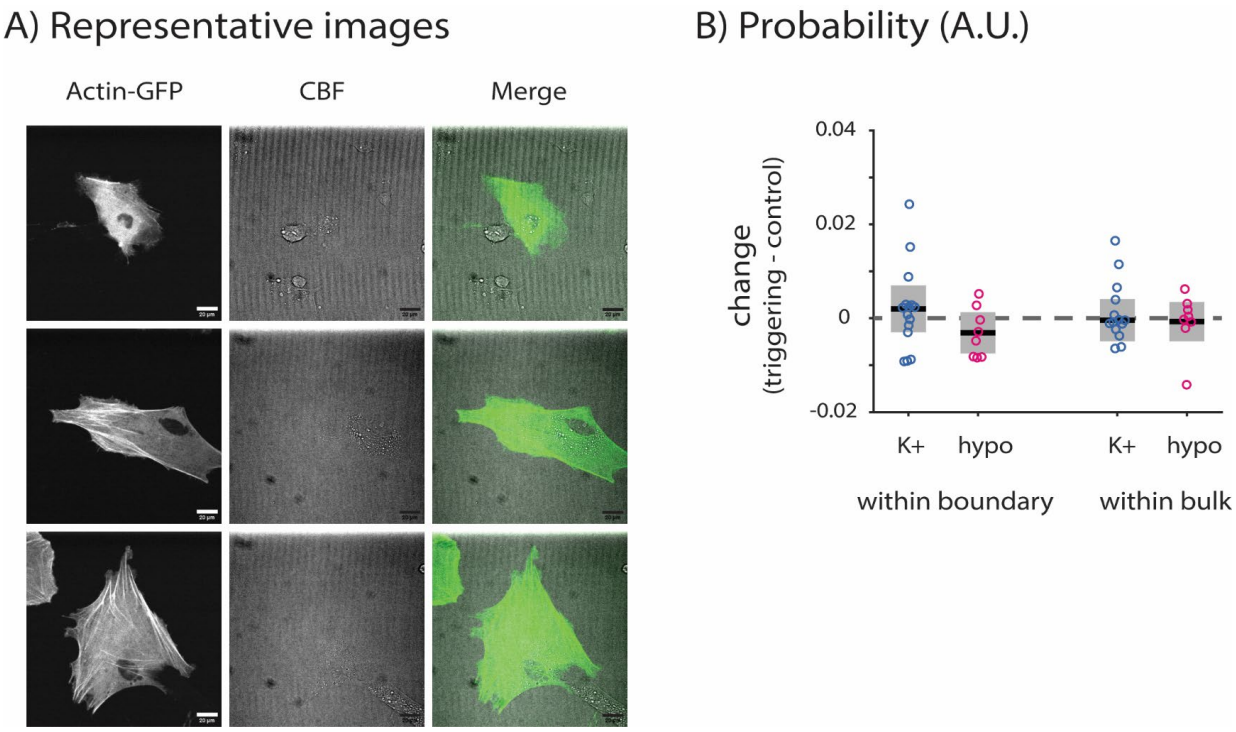

1357

1358

1359 **Fig. 1 – figure supplement 1: Representative images of primary astrocytes and**

1360 **supplementary data.**

1361 **A)** Three representative images of primary astrocytes grown on PDL-coated glass (PDL).

1362 **B)** Probability of actin dynamics within boundary (p=0.402 for control vs. K+, p=0.138 for control

1363 vs. hypo) and within bulk (p=0.854 for control vs. K+, p=0.742 for control vs. hypo). P-values

1364 determined by paired t-test. n=15 paired cells for control and K+, and n=8 paired cells for control

1365 and hypo. Grey boxes indicate 95% confidence intervals. Solid black lines indicate mean.

1366

1367

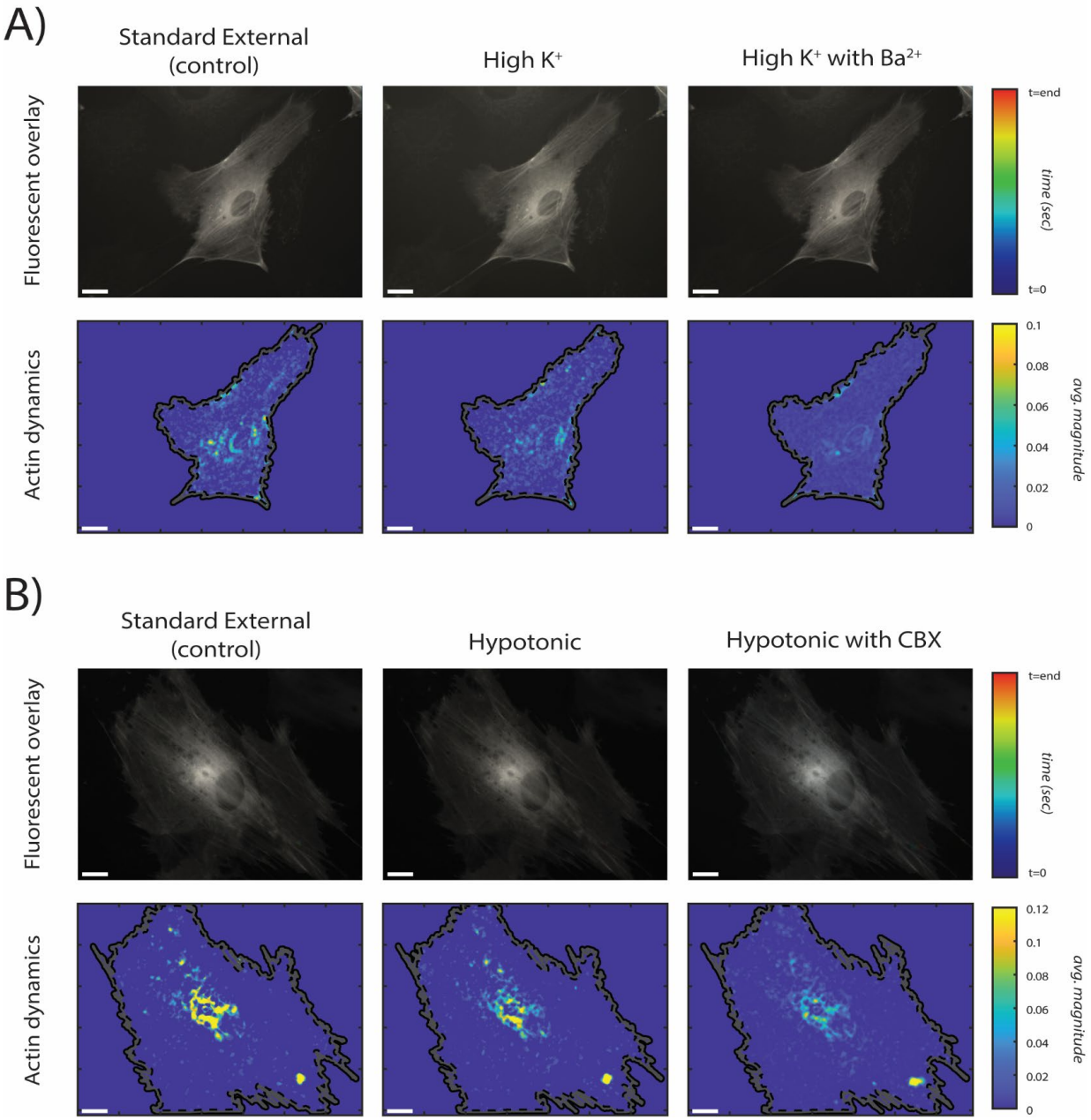

1368
1369

1370 **Fig. 1 – figure supplement 2: Representative images and analysis of actin dynamics after**

1371 **pharmacologic perturbations.**

1372 **A)** Representative actin-GFP timelapse overlays (top row) and quantified actin dynamics (bottom

1373 row) after triggering with high K^+ and subsequently blocking potassium channels with barium

1374 (Ba^{2+}). Left to right: representative astrocyte in standard external (control), high K^+, and high K^+

1375 with Ba^{2+}. **B)** Representative actin-GFP timelapse overlays (top row) and quantified actin
1376 dynamics (bottom row) after triggering with hypotonic and subsequently blocking gap junctions
1377 with carbenoxolone (CBX). Left to right: representative astrocyte in standard external (control),
1378 hypotonic, and hypotonic with CBX. Top rows: colorbar indicates time. Bottom rows: colorbar
1379 indicates average optical flow magnitude. Scalebars indicate 20 μm.
1380

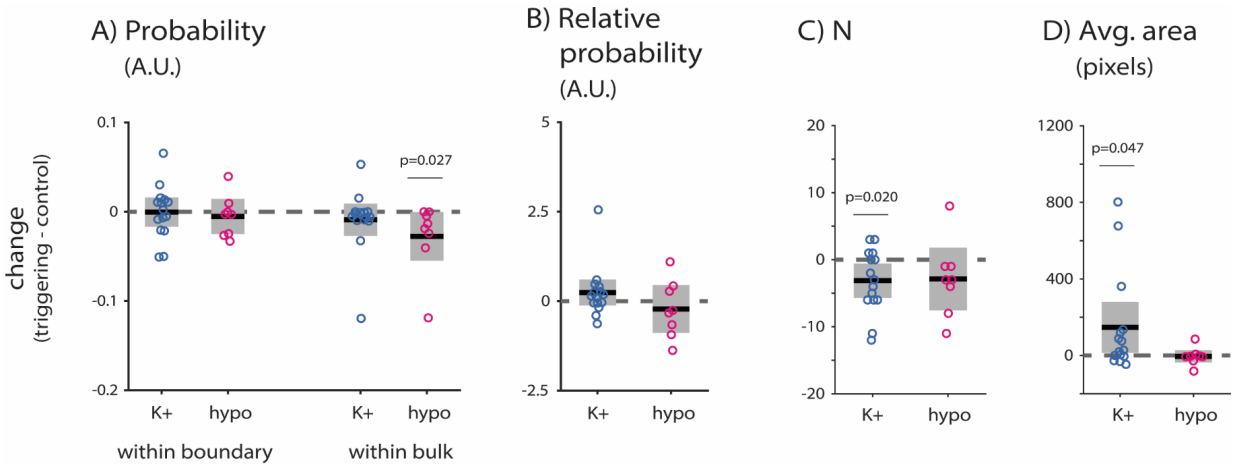

Fig. 2 – figure supplement 1: Additional parameters characterizing differences in actin dynamics within hotspot regions after chemical triggering.

A) Probability of hotspot dynamics within boundary (p=0.969 for control vs. K+, p=0.557 for control vs. hypo) and within bulk (p=0.847 for control vs. K+, p=0.027 for control vs. hypo). **B)** Relative probability of hotspot dynamics (p=0.215 for control vs. K+, p=0.462 for control vs. hypo). **C)** Number of hotspots (p=0.020 for control vs. K+, p=0.189 for control vs. hypo). **D)** Average size of hotspots (p=0.047 for control vs. K+, p=0.794 for control vs. hypo). P-values determined by paired t-test. n=15 paired cells for control and K+, and n=8 paired cells for control and hypo. Grey boxes indicate 95% confidence intervals. Solid black lines indicate mean.

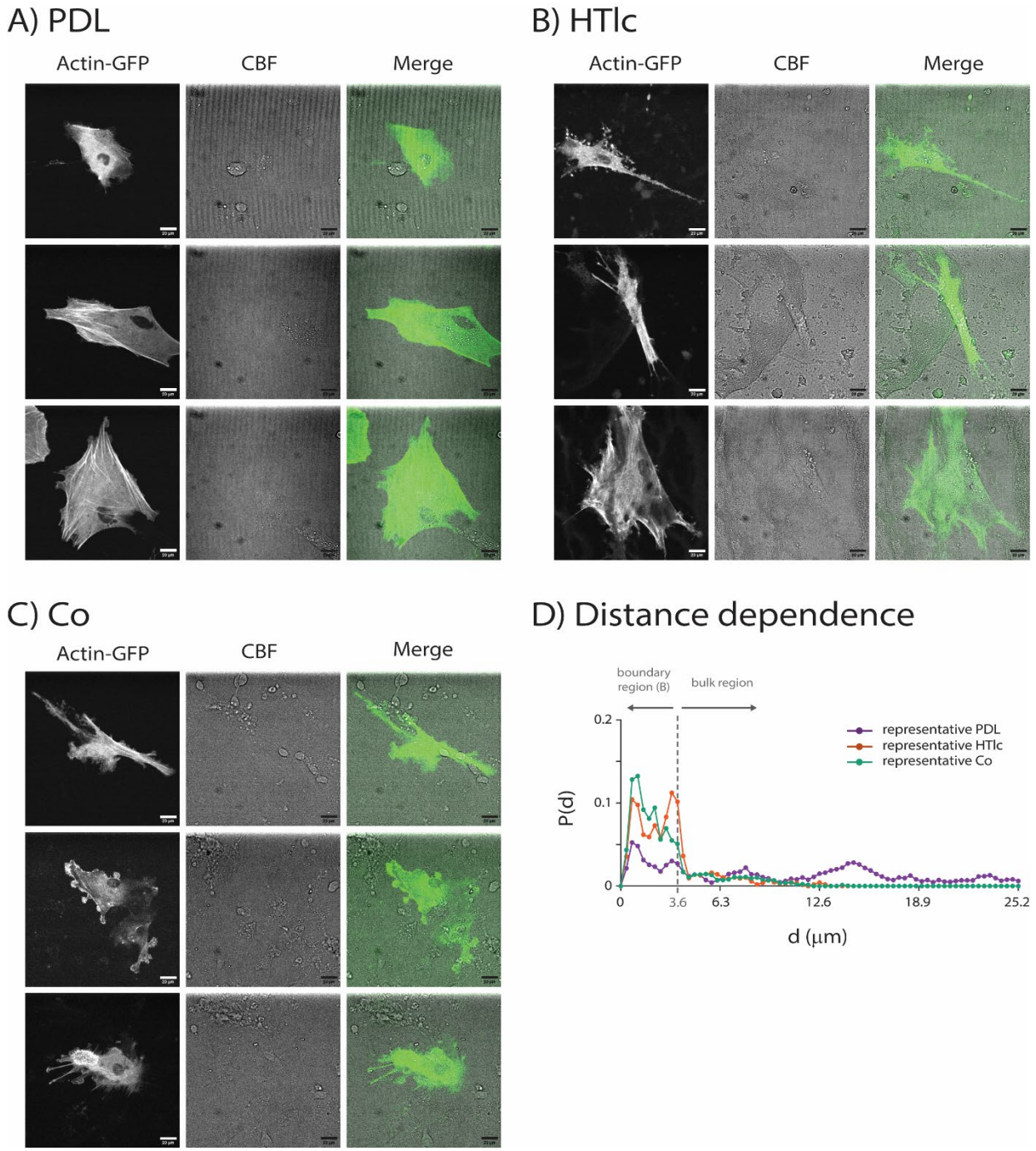

Fig. 3 – figure supplement 1: Representative images of primary rat astrocytes in three culturing conditions and supplementary data.

A) Three representative images of primary astrocytes grown on PDL-coated glass (PDL). **B)** Three representative images of primary astrocytes grown on HTlc nanotopographic films (HTlc).

1401 **C)** Three representative images of primary astrocytes co-cultured with neurons (Co) on PDL-
1402 coated glass. Left columns show images of astrocytes transduced with actin-GFP from the 488 nm
1403 channel. Middle columns show confocal brightfield (CBF) images. Right columns show the merge
1404 of 488 nm and CBF channels. Scalebars indicate 20 μm. **D)** Full distance curves for representative
1405 PDL, HTlc, and Co cells shown in **Figure 3A**.
1406

1407

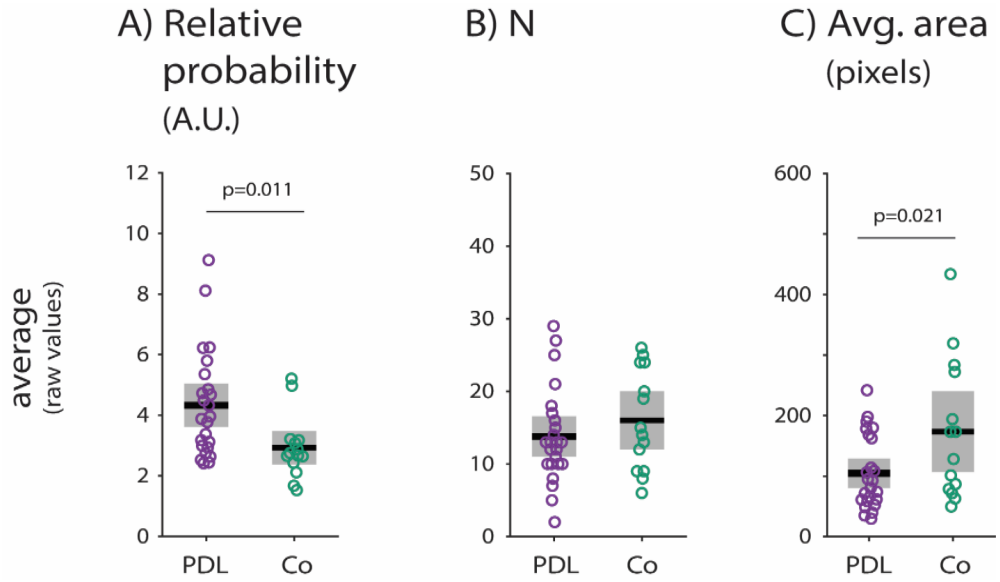

1408
1409

1410 **Fig. 4 – figure supplement 1: Additional parameters characterizing how the presence of**

1411 **neurons alters actin dynamics within hotspots.**

1412 **A)** Relative probability of hotspot dynamics (p=0.011 for PDL vs. Co). **B)** Number of hotspots

1413 (p=0.333 for PDL vs. Co). **C)** Average size of hotspots (p=0.021 for PDL vs. Co). P-values

1414 determined by two-sample t-test. n=24 cells for PDL, and n=14 cells for Co. Grey boxes indicate

1415 95% confidence intervals. Solid black lines indicate mean.